

Entanglement properties of optomagnonic crystal from nonlinear perspective

M. Wanic,¹ C. Jasiukiewicz,¹ Z. Toklikishvili,² V. Jandieri,³
M. Trybus,¹ E. Jartych,⁴ S. K. Mishra,⁵ and L. Chotorlishvili¹

¹*Department of Physics and Medical Engineering,
Rzeszów University of Technology, 35-959 Rzeszów, Poland*

²*Faculty of Exact and Natural Sciences, Tbilisi State University, Chavchavadze av.3, 0128 Tbilisi, Georgia*

³*General and Theoretical Electrical Engineering (ATE), Faculty of Engineering,
University of Duisburg-Essen and CENIDE - Center for Nanointegration Duisburg-Essen, D-47048 Duisburg, Germany*

⁴*Lublin University of Technology, Department of Electronics and Information Technology,
Faculty of Electrical Engineering and Computer Science, 20-618 Lublin, Poland*

⁵*Department of Physics, Indian Institute of Technology (Banaras Hindu University) Varanasi - 221005, India*
(Dated: June 14, 2024)

Optomagnonics is a new field of research in condensed matter physics and quantum optics focused on strong magnon-photon interactions. Particular interest concerns realistic, experimentally feasible materials and prototype cheap elements for futuristic nanodevices implemented in the processing or storing of quantum information. Hence, magnon-photon entanglement is an essential ingredient since it allows manipulation and control of the quantum states of bipartite systems. Quantifying the entanglement between two continuous bosonic modes, such as magnons and photons, is not trivial. The state-of-the-art for today is the logarithmic negativity, calculated through the quantum Langevin equations subjected to thermal noise. However, due to its complexity, this method requires further approximation. Namely, after the linearization procedure, quantum operators are replaced by their semiclassical expectation values calculated near the steady state. The cost of this approximation is the loss of information about the phases of propagated quantum states. In the present work, we propose a new procedure that avoids the linearization of dynamics. Prior analyzing the quantum entanglement, we explore the nonlinear semiclassical dynamics in detail and precisely define the phase space. The typical nonlinear dynamical system holds bifurcation points and fixed points of different characters in its phase space: Saddle points, Stable and unstable spiral, and Stable node points. Here, we show that methods of the qualitative theory of nonlinear differential equations are also relevant for optomagnonic problems. Our main finding is that entanglement is not defined in the Saddle Point region. On the other hand, the maximum of the entanglement corresponds to the region near the border between the Stable node and Stable spiral regions. Our approach is quite general. However, in numerical calculations, we considered a particular system: optomagnonic crystal based on the yttrium iron garnet (YIG) slab with the periodic air holes drilled in the slab. In our case, Magnon-photon interaction occurs due to the magneto-electric effect in YIG. We provide explicit derivation of the coupling term. Besides, we calculate photon modes for a particular geometry of the optomagnonic crystal. We analyzed the amplitude-frequency characteristics of the optomagnonic crystal and showed that due to the instability region, one could efficiently switch the mean magnon numbers in the system and control entanglement in the system. We discovered that the zero-entanglement region is characterized by the singularity in the covariance matrix and corresponds to the Saddle fixed point region of the dynamical system. We also studied the dependence of magnon-photon entanglement on the temperature and showed that the region of the nonzero entanglement shrinks at higher temperatures. Our primary finding is that the covariance matrix has singularities in the Saddle fixed point region, and therefore, entanglement is not defined in the same region. The entanglement is nonzero in the Stable fixed point region.

I. INTRODUCTION

Optomagnonics is the research topic formed during the last decade where fundamental quantum physics and technological applications met and have been developing together, mutually enriching each other with new ideas and novel technological solutions [1–5]. Quantum computation and functionality tasks on the nanoscale level raised specific requirements for the systems. Typically, platforms designed for quantum information protocols are binary, constituent of two different subsystems, and incorporate different parameters. While nanomechanical systems joint mainly mechanical and spin excitations [6–8], constituent parts of optomagnonic sys-

tems are photons and magnons. Optomagnonics follows the spirit of nanomechanics and nanomechanical systems, merging quantum optics and solid-state physics. Photon-phonon interaction in photonic crystals plays a crucial role in the entanglement properties [9–13]. Interest in optomagnonics concerns the enhanced interactions between magnons and photons. Previous studies showed that entanglement between two continuous bosonic modes requires interactions beyond the bilinear form [14, 15]. The paradigmatic optomagnonic setup is an optical cavity and a yttrium iron garnet (YIG) sphere. Magnetocrystalline anisotropy in the YIG sphere leads to the nonlinear magnon interaction and Magnon Kerr Effect (MKE) [16–21]. The interaction term $K_0 \hat{m}^+ \hat{m} \hat{m}^+ \hat{m}$,

(where \hat{m}^+ , \hat{m} are magnon creation and annihilation operators) is usually small, characterized by the interaction constant $K_0 = \mu_0 K_{0an} \gamma_e / M^2 V_m$, with μ_0 , being the magnetic permeability, K_{0an} the anisotropy constant, γ_e the gyromagnetic ratio M the saturation magnetization, and V_m is the volume of the YIG sphere. The smaller the volume of the YIG sphere, the stronger the MKE is. In the present work, we propose the model of optomagnonic crystal and study magnon-photon entanglement based on the magnon condensation effect. We consider a YIG slab with a periodic array of holes in the YIG slab. To quantify entanglement between two continuous bosonic modes [22–24] (photonic and magnonic), we exploit measures of the entanglement such as logarithmic negativity [25, 26]. Instead of the YIG sphere and weak Kerr effect, we propose to exploit the magnon condensation effect and intraband magnon-magnon interaction originated from the perpendicular magnetocrystalline anisotropy (PMA) and bismuth doping on the YIG slab. The magnon-magnon interband interaction term in the magnon condensate mimics the effective Kerr effect. We propose to control of the effective Kerr nonlinearity through the doping of the YIG slab by bismuth impurities. Utilizing the multiferroic properties of YIG [27] and magnetoelectric effect (ME) [28, 29], we derive photon-magnon coupling in terms of the effective Dzyaloshinskii-Moriya (DM) interaction [30–33]. The effective DM interaction and magnon condensation effect allow us to control nonlinearity in the system through two parameters: external electric field and concentration of the doped bismuth impurities.

The study of magnon-photon entanglement at finite temperatures requires the method of the quantum Langevin equation. Due to the complexity of this approach, a certain approximation is needed. Namely, general quantum operator \hat{Q} is replaced by $\hat{Q} = \langle \hat{Q} \rangle + \delta \hat{Q}$, where $\delta \hat{Q}$ is the deviation of operators from its steady state expectation value $\langle \hat{Q} \rangle$. In particular, magnon creation and annihilation operators are replaced by $\langle \hat{m}^\dagger \rangle = \beta^* e^{-i\varphi}$, $\langle \hat{m} \rangle = \beta e^{i\varphi}$. While the mean magnon number is given by $\langle \hat{m}^\dagger \hat{m} \rangle = |\beta|^2$, the phase φ is considered as a free parameter in the linear theory. The present work shows that phase plays a crucial role in nonlinear cases, leading to the instability and transitions between the different dynamical regimes. We apply methods of the dynamical system's theory and find bifurcation points and different dynamical regions in the system's phase space. We show that separatrix lines separate those regions, and magnon-photon entanglement differs in the topologically distinct regions of the phase space. The qualitative theory of ordinary differential equations is based on the phase space analysis. The standard procedure implies linearization of the system in the vicinity of the fixed point, which corresponds to the system's steady state. However, the non-equilibrium initial state can be prepared by pumping magnonic excitations using the nanoantenna. Non-equilibrium effects are also in the scope of our interest. Therefore, when analyzing nonlinear effects, we exploit

more general formalism and study the system's phase space in the vicinity of the steady state fixed point and in the vicinity of non-equilibrium states. The manuscript is organized as follows: Section II describes the model. In section III, we present results of calculations for photonic modes. In section IV, we consider the system's semiclassical approach and nonlinear dynamical aspect. In section V, we analyze magnon-photon entanglement in the system and conclude the work.

II. MODEL

The effect of magnon condensation was discovered about twenty years ago [34]. Afterward, magnon condensation was observed in YIG [35]. The interaction between magnons is weak at low densities of the condensate but becomes significant at higher magnon densities. Magnon condensate is stable when magnons repel each other. The stability of the magnon condensate is granted by dipole-dipole interaction between magnetic moments and is associated with the enhancement of the band depth [36]. We consider the YIG slab in the XOY plane. Equilibrium magnetization is oriented along \mathbf{x} axis, parallel to the applied constant magnetic field $H_0 \mathbf{x}$ as shown in Fig.1. The PMA is oriented in the \mathbf{z} direction $H_{an} = -K_{an} \sum_n (\mathbf{m}_n \mathbf{z})^2$. The effective Hamiltonian of the magnetic subsystem takes the form [37]:

$$\hat{H}_m = \omega \hat{m}^\dagger \hat{m} + K \hat{m}^\dagger \hat{m} \hat{m}^\dagger \hat{m}. \quad (1)$$

Here, $\omega = \sqrt{\eta_1^2 - \eta_2^2}$, with $\eta_1 = Jq^2 + \gamma_e(H_{0x} + 2\pi M_s f_q) - K_{an} S$ and $\eta_2 = 2\pi M_s f_s - K_{an} S$ is the magnon frequency, which is in the order of several GHz, $S = 14$ is the YIG spin per unit cell, J is the exchange constant, M_s saturation magnetization, f_q form factor, γ_e is gyromagnetic ratio, \hat{m}^\dagger , \hat{m} are magnon creation annihilation operators, q is the magnon wave vector. We chose a particular magnon mode with wave vector $q = 25\mu m^{-1}$ corresponding to the concave shape of the magnon band (a deep stable minimum) in the magnon condensate [37]. For the applied magnetic field $H_0 = 1\text{kOe}$ and $K_{an} = 0.8\mu eV$, the frequency of magnons in the condensate is equal to $\omega = 2\text{GHz}$. We set dimensionless parameters by introducing the dimensionless time $t = \tau\omega$. The dimensionless Hamiltonian $\hat{H}/\hbar\omega$. Hereafter, the energy scale is given by $\hbar\omega$. The second term in Eq.(1) describes the intraband magnon-magnon interaction. The interaction constant K in Eq.(1) has the form [37]: $K = -\frac{\gamma_e \pi M_s}{SN} [(\alpha_1 + \alpha_3)f_Q - 2\alpha_2(1 - f_{2Q})] - \frac{JQ^2}{2SN}(\alpha_1 - 4\alpha_2) + \frac{K_{an}}{2N}(\alpha_1 + \alpha_3)$. Here N is the total number of spin sites, Q is the wave vector of the condensate magnons, $\alpha_{1,2}$ are Bogoliubov transformation coefficients. The last term is the PMA $H_{an} = -K_{an} \sum_n (\mathbf{m}_n \mathbf{z})^2$. The value of K_{an} can be controlled by bismuth doping. For more details about magnon spectrum and intraband magnon-magnon interaction term we refer to the work [37]. We note that

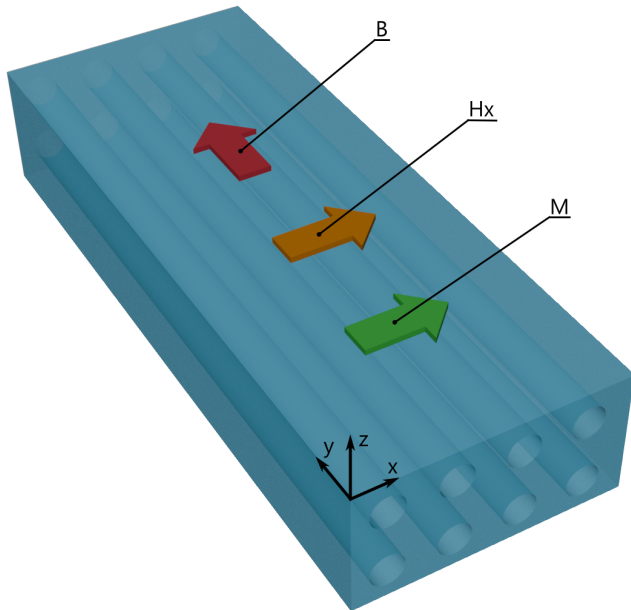


FIG. 1. The optomagnonic crystal is based on the YIG slab, with the periodic chain composed of the air holes having a radius $a = 0.46h$ (h is the period of the structure). The perpendicular magnetocrystalline anisotropy (PMA) oriented in the \mathbf{z} direction $H_{an} = -K_{an} \sum_n (\mathbf{m}_n \mathbf{z})^2$, and constant mag-

netic field $\mathbf{H} = \mathbf{x}H_x$ applied along the \mathbf{x} axis lead to the ground state magnetization $\mathbf{m}_n = \mathbf{M}_n/|\mathbf{M}_n|$ along the \mathbf{x} axis. The time-dependent magnetic field $B(t) = B \cos \omega_0 t$ is applied along the \mathbf{y} axis. Due to the geometry of the YIG slab $L_y \gg L_{x,z}$, $k_{x,y,z} = \pi/L_{x,y,z}$, $k_y y \approx 0$ the leading mode is $U_y = U_0 \sin(k_x x) \sin(k_z z)$. The leading photonic mode $\mathbf{E}_y = iU_y (\hat{a} - \hat{a}^\dagger)$ couples the magnonic mode of the magnon condensate through the magneto-electric (ME) effect $H_{DM} = \mathbf{E} \cdot \mathbf{P} = E_y P_y$. Here \mathbf{P} is the ferroelectric polarization [27]: $\mathbf{P} = g_{ME} \mathbf{e}_{n,n+1} \times \mathbf{m}_n \times \mathbf{m}_{n+1}$ in YIG, $\mathbf{e}_{n,n+1}$ is the unit vector connecting adjacent magnetic moments \mathbf{m}_n and \mathbf{m}_{n+1} , \hat{a} are the photon creation and annihilation operators, and g_{ME} is the ME coupling constant. Due to the geometry of the optomagnonic crystal, the only nonvanishing coupling term is the z component of the vector chirality given by $\hat{H}_{DM} = ig_{ME} U_y \mathbf{e}_y \cdot \mathbf{e}_x \times (\mathbf{m}_n \times \mathbf{m}_{n+1})_z (\hat{a} - \hat{a}^\dagger)$, because the second term with $\mathbf{e}_z \times (\mathbf{m}_n \times \mathbf{m}_{n+1})_x$ is zero due to the orientation of the ground state magnetization vector along the x axis.

PMA and, consequently, nonlinearity constant K can be controlled not only through bismuth doping but also using straintronics methods, i. e., by applying mechanical stress. For more details we refer to the review paper [38] and references therein.

Magnon-photon coupling in our model arises because of the ME effect in YIG. Derivation of the magnon-photon coupling term because of ME coupling is described in details in [15]. The essence of our optomagnonic crystal is the coupling between photons and magnons through the effective DM term [33, 39–42]. Tak-

ing into account ME effect in YIG [27], we couple quantized cavity field $\mathbf{E} = i\mathbf{U}(\mathbf{r}) (\hat{a} - \hat{a}^\dagger)$ with the emergent ferroelectric polarization $\mathbf{P} = g_{ME} \mathbf{e}_{n,n+1} \times \mathbf{m}_n \times \mathbf{m}_{n+1}$ in YIG, i.e., $H_{DM} = \mathbf{E} \cdot \mathbf{P}$. Here $\mathbf{m}_n = \mathbf{M}_n/|\mathbf{M}_n|$ is the normalized magnetic moment, $\mathbf{e}_{n,n+1}$ is the unit vector connecting adjacent magnetic moments \mathbf{m}_n and \mathbf{m}_{n+1} , \hat{a}^\dagger , \hat{a} are the photon creation and annihilation operators, and g_{ME} is the ME coupling constant [27]. The cavity mode function $\mathbf{U}_l(\mathbf{r})$ is the solution of the Helmholtz equation $\Delta U_{x,y,z} + k^2 U_{x,y,z} = 0$. In the experiment one drills the cylindrical holes in the YIG slab along \mathbf{y} axis as shown in Fig.1. Due to the Coulomb gauge $\nabla \cdot \mathbf{U} = 0$ and elongated along the \mathbf{y} axis structure of the optomagnonic crystal, i.e., $L_y \gg L_{x,z}$, $k_{x,y,z} = \pi/L_{x,y,z}$, $k_y y \approx 0$ the leading mode is $U_y = U_0 \sin(k_x x) \sin(k_z z)$, and therefore the coupling term takes the form $\hat{H}_{DM} = ig_{ME} U_y \mathbf{e}_y \cdot \mathbf{e}_x \times (\mathbf{m}_n \times \mathbf{m}_{n+1})_z (\hat{a} - \hat{a}^\dagger)$. At the next step we exploit Holstein-Primakoff transformation [43] and rewrite coupling term using magnon's bosonic operators $\hat{H}_{DM} = iD\hat{m}^\dagger \hat{m} (\hat{a} - \hat{a}^\dagger)$, where $D = 4Sg_{ME} U_y \sin(k)$, $S = 14$ is the YIG spin per unit cell [44], k is the magnon wave vector, and D is the effective DM constant. Thus, the value of the effective DM constant D can be controlled dynamically by varying the strength of an applied high-frequency laser field. The critical issue is that the ME effect is based on the hopping processes [27] and that time-periodic fields renormalize the electronic tunneling, leading to the effective rescaled DM. This mechanism is discussed in detail in [45, 46].

The Hamiltonian of the photonic subsystem has the form $\hat{H}_f = \omega_f \hat{a}^\dagger \hat{a}$. Details about the photonic subsystem are presented in the next section. Here, at the current stage, we are ready to compile the Hamiltonian of the total system:

$$\hat{H}_{tot} = \omega_f \hat{a}^\dagger \hat{a} + \omega \hat{m}^\dagger \hat{m} + K \hat{m}^\dagger \hat{m} \hat{m}^\dagger \hat{m} + iB (\hat{m}^\dagger e^{-i\omega_0 t} - \hat{m} e^{i\omega_0 t}) + iD \hat{m}^\dagger \hat{m} (\hat{a} - \hat{a}^\dagger). \quad (2)$$

Here B , ω_0 are the amplitude and frequency of the time dependent magnetic field applied along y axis.

III. PHOTONIC CAVITY

The geometry of the problem is shown as inset in Fig. 2. The structure composed of periodically distributed air-holes with circular section and radius a and relative dielectric permittivity ϵ_c ($\epsilon_c = 1$) is geometrically invariant along the y -axis and infinite and periodic with a period h along the x -axis. The surrounding medium is material with a relative dielectric permittivity ϵ_b and permeability μ_0 . The structure is located in the free space. Applying the addition theorem for the cylindrical functions and using the boundary condition on the surfaces of the circular rod at the global origin, a simple dispersion equation for the eigenmodes is obtained in the following form:

$$\det[\mathbf{I} - \mathbf{T}(k_c a, k_b a) \mathbf{L}(k_b h, k_{x0} h)] = 0, \quad (3)$$

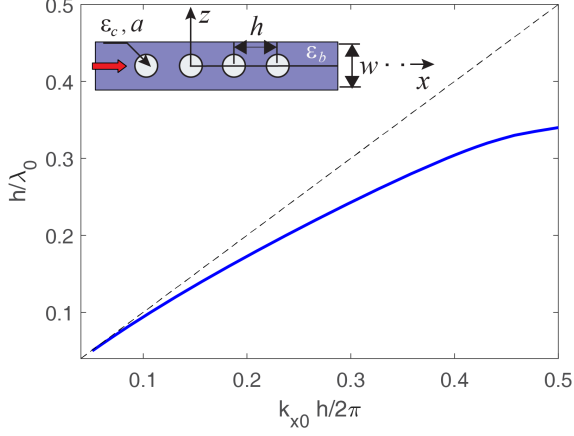


FIG. 2. Brillouin diagram of the fundamental TM mode of the periodic chain composed of the air-holes having a radius $a = 0.46h$ (h is period of the structure) and situated in the background medium with the relative dielectric permittivity $\epsilon_b = 5$. The thickness of the slab is $w = h$, and λ_0 is the wavelength in the free space. The dashed line defines the light line. To control the frequency of the photons, we tune the wavelength at the fixed period of the structure h . We are interested in the GHz frequency range and the desired frequency can be easily determined from the dispersion diagram that is shown in non-dimensional parameters. For $h = 10\text{mm}$, photon frequency is the order of $\omega_f = 5\text{GHz}$.

where \mathbf{I} is the unit matrix. The transition matrix $\mathbf{T}(k_c a, k_b a)$ (T-matrix), which describes the nature of this particular scatterer, can be written in a compact form in terms of a diagonal matrix. It is given for the TM wave (E_y, H_x, H_z) and the TE wave (H_y, E_x, E_z) in the closed form:

$$T_m^{\text{TE}} = \frac{-\sqrt{\epsilon_b} J_m \tilde{J}'_m + \sqrt{\epsilon_c} J'_m \tilde{J}_m}{\sqrt{\epsilon_b} H_m^{(1)} \tilde{J}'_m - \sqrt{\epsilon_c} H_m^{(1)'} \tilde{J}_m} \quad (4)$$

$$T_m^{\text{TM}} = \frac{-\sqrt{\epsilon_b} \tilde{J}_m J'_m + \sqrt{\epsilon_c} J_m \tilde{J}'_m}{\sqrt{\epsilon_b} H_m^{(1)'} \tilde{J}_m - \sqrt{\epsilon_c} H_m^{(1)} \tilde{J}'_m} \quad (5)$$

Here $J_m(k_b a)$, $\tilde{J}_m(k_c a)$, and $H_m^{(1)}(k_b a)$ are Bessel and Hankel functions of the m -th order, respectively, the prime notation denotes their derivatives concerning the arguments, $k_b = \omega \sqrt{\mu_0 \epsilon_0 \epsilon_b}$ and $k_c = \omega \sqrt{\mu_0 \epsilon_0 \epsilon_c}$ are the wavenumbers in the background medium and air-hole respectively, ω is the angular frequency. Note that the Fresnel matrices are the diagonal matrices implemented

in the analysis on the upper ($w = h$) and lower ($w = 0$) boundaries of the structure (see inset in Fig.2). The modal field in a periodic chain can be expressed in terms of an infinite series of space harmonics, each having a complex propagation wavenumber $k_{xn} = \beta_n + i\alpha$, with $\beta_n = k_{x0} + 2\pi n/h$ and $n = 0, \pm 1, \pm 2, \dots$. The n -th space-harmonic along the transverse z -axis behaves as $e^{j k_{zn} |z|}$, where $k_{zn} = \sqrt{k_0^2 - k_{xn}^2}$ is the relevant wavenumber. The formalism presented in the paper allows for the appropriate choice of the proper or improper spectral determination (positive or negative sign for $\text{Im}(k_{yn})$, respectively) for each space harmonic [47, 48].

Lattice-Sums. Lattice Sums that appear in the dispersion equation for the eigenmodes play a crucial role in our formalism. It is expressed through the infinite series of the Hankel functions. It does not depend on the polarization of the incident field, the location of the observation points, and the material properties of the scatterers. Hence, it represents a very efficient technique for solving periodic structures' electromagnetic scattering problems. The m -th component of the Lattice Sums is given in the following form [47–49]:

$$L_m = \sum_{n=1}^{\infty} H_m^{(1)}(k_b n h) [\exp(ink_{x0} h) + (-1)^m \exp(-ink_{x0} h)]. \quad (6)$$

The series converges very slowly for the real k_{x0} and diverges for the complex k_{x0} . In order to speed up the calculation, applying the Ewald transformation, the Lattice Sums can be calculated as a sum of the spectral and the spatial series [47, 48]. The details of derivation are omitted in the work, we give here the final expressions for each term of the Lattice Sums:

$$L_m^{\text{spectral}} = \frac{1}{k_{zn}} \times \sum_{n=-\infty}^{\infty} \left(\frac{k_{xn}}{k_b} \right)^m \sum_{q=0}^{[m/2]} (-1)^q \binom{m}{2q} \left(\frac{k_{zn}}{k_{xn}} \right)^{2q} C_{q,n}, \quad (7)$$

with

$$C_{q,n} = \frac{1}{k_{zn}} \times \text{erfc} \left(-i \frac{h k_{zn}}{2 E_{spl}} \right) \frac{e^{\frac{h^2 k_{zn}^2}{4 E_{spl}^2}}}{k_{zn}} \sum_{s=1}^q \frac{\left(-i \frac{h k_{zn}}{2 E_{spl}} \right)^{1-2s}}{\Gamma(1.5 - s)}, \quad (8)$$

and

$$L_m^{spatial} = \delta_{m0} \left[-1 - \frac{i}{\pi} Ei \left(\frac{k_b^2 h^2}{4E_{spl}^2} \right) \right] + \frac{2^{m+1}}{i\pi} \sum_{n=1}^{\infty} [\exp(ink_{x0}h)] \quad (9)$$

$$+ (-1)^m \exp(-ink_{x0}h) \left(\frac{n}{k_0 h} \right)^m \int_{E_{spl}}^{\infty} d\eta \frac{\exp \left(-n^2 \eta^2 + \frac{h^2 k_b^2}{4\eta^2} \right)}{\eta^{-2m+1}}. \quad (10)$$

Here $\text{erfc}(\dots)$ is the error function. In the numerical results that follow, the Ewald splitting parameter $E_{spl} = \sqrt{\pi}$. The proposed formalism gives Gaussian convergence even in the case of complex and leaky waves [47–49]. Yasumoto presented another efficient method based on a simple trapezoidal integration formulae [49]. Although the authors mention that their method works only for the real propagation constant k_{x0} , the identity theorem in the complex analysis allows us to calculate the Lattice Sums for the complex k_{x0} . However, the main advantage of the formalism in this work is that it allows for the appropriate choice of the spectral determination for each space harmonic (choice of a sign for k_{zn}), which is not the case in [49]. Although for the mode analysis, we calculate only the bound modes (k_{x0} is a real value), the determination of each space-harmonic is essential for a flexible design of Fabry-Perot cavities, EBG-based resonators, open waveguides or plasmonic guiding devices with intrinsic losses.

IV. NONLINEAR DYNAMICS

Nonlinearity can substantially influence the dynamic properties of the system [50–52]. Following [14, 15], we derive the set of quantum Langevin equations (QLEs) describing the system:

$$\begin{aligned} \frac{d\hat{a}(t)}{dt} &= -i [\hat{a}(t), \hat{H}_{tot}] - \gamma_f \hat{a}(t) + \sqrt{2\gamma_f} \hat{a}_{in}(t), \quad (11) \\ \frac{d\hat{m}(t)}{dt} &= -i [\hat{m}(t), \hat{H}_{tot}] - \gamma_m \hat{m}(t) + \sqrt{2\gamma_m} \hat{m}_{in}(t). \end{aligned}$$

Here, γ_f and γ_m are damping constants for cavity photons and magnons, respectively. For a high fineness optomagnonic crystal, damping constants are small. Here $a_{in}(t)$, $m_{in}(t)$ are input noise bosonic operators for the photonic and magnonic subsystems respectively, characterized by the correlation functions $\langle a_{in}^\dagger(t) a_{in}(t') \rangle = N_a(\omega_f) \delta(t-t')$, and $\langle m_{in}^\dagger(t) m_{in}(t') \rangle = N_m(\omega) \delta(t-t')$, where $N(\omega) = [\exp(\hbar\omega/k_B T) - 1]^{-1}$ is the Bose-Einstein distribution function. In Eq.(11) we implement semiclassical and rotating wave approximations through the transformations $O = \langle \hat{O} \rangle$, $(\hat{a} - \hat{a}^+) \hat{m} = (a - a^*) m$, $\langle \hat{m}^+ \hat{m} \rangle = |m|^2$, $\hat{m} \rightarrow \hat{m} e^{-i\omega_0 t}$, $\hat{m}_{in} \rightarrow m_{in} e^{-i\omega_0 t}$ and

$a \equiv |a| e^{i\phi} = \alpha e^{i\phi}$, $m \equiv |m| e^{i\varphi} = \beta e^{i\varphi}$ and deduce:

$$\begin{aligned} \dot{\alpha} &= -D\beta^2 \cos \phi - \gamma_f \alpha, \\ \dot{\phi} &= -\omega_f + \frac{D\beta^2}{\alpha} \sin \phi, \\ \dot{\beta} &= -\gamma_m \beta + B \cos \varphi, \\ \dot{\varphi} &= \omega - \omega_0 + 2D\alpha \sin \phi - 2K\beta^2 - \frac{B \sin \varphi}{\beta}. \quad (12) \end{aligned}$$

When studying entanglement properties, most of the authors linearize Eq.(11), e.g., [14, 15] and references therein. Therefore, the information about the phases ϕ and φ is lost. Phases are chosen according to particular assumptions. Here, we proceed with nonlinear system Eq.(12) and implement methods of Dynamical system's theory [53]. The fixed point of the dynamical system Eq.(12) is given by:

$$\begin{aligned} \alpha^2 &= \frac{D\beta^4}{\omega_f^2 + \gamma_f^2}, \\ \phi &= -\arctan(\omega_f/\gamma_f), \\ \Delta_m [\gamma_m^2 + (\omega_0 - \omega + \Delta_m)^2] &= \left(\frac{2D^2\omega_f}{\omega_f^2 + \gamma_f^2} - 2K \right) B^2, \\ \tan \varphi &= \frac{\omega_0 - \omega + 2D\alpha \sin \phi - 2K\beta^2}{\gamma_m}. \quad (13) \end{aligned}$$

Here $\Delta_m = \beta^2 \delta_K$, $\delta_K = \left(\frac{2D^2\omega_f}{\omega_f^2 + \gamma_f^2} - 2K \right)$. Eq.(13) is the essence of a nonlinear set of equations with respect to the variables: $\alpha(D, B, K)$, $\beta(D, B, K)$, $\phi(D, B, K)$, $\varphi(D, B, K)$. The amplitude-frequency characteristics of the nonlinear resonance follow the singular points where the derivative with respect to the detuning $\delta\omega = \omega_0 - \omega$ turns to be zero [54]

$$\frac{d}{d\delta\omega} \{ \Delta_m [\gamma_m^2 + (\Delta_m + \delta\omega)^2] \} = 0. \quad (14)$$

From Eq.(14), we derive the equation of the amplitude-frequency characteristics.

$$\frac{d\beta^2}{d\delta\omega} = - \frac{2\beta(\delta_k \beta^2 + \delta\omega)}{3(\delta_k \beta^2)^2 + 4\delta_k \beta^2 \delta\omega + \gamma_m^2 + \delta\omega^2}. \quad (15)$$

The singular points correspond to the case $3(\delta_k \beta^2)^2 + 4\delta_k \beta^2 \delta\omega + \gamma_m^2 + \delta\omega^2 = 0$. i.e., frequencies:

$$\delta\omega_{1,2} = -2\delta_k \beta^2 \mp \sqrt{(\delta_k \beta^2)^2 - \gamma_m^2}. \quad (16)$$

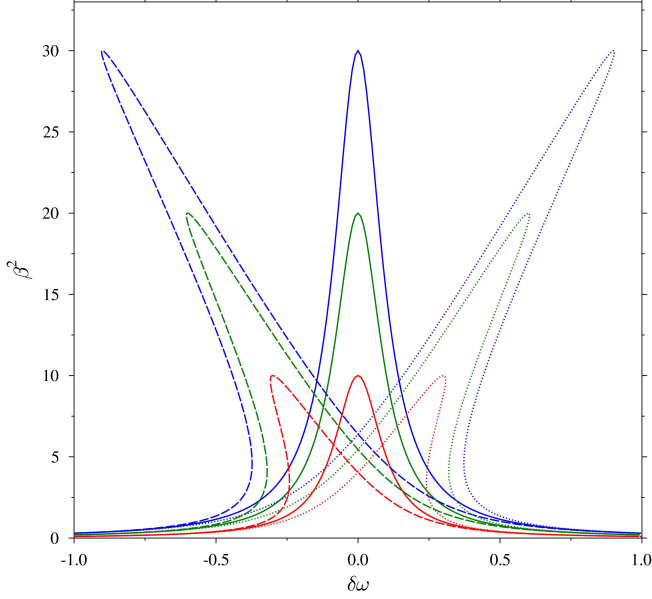


FIG. 3. Dependence of the steady-state mean magnon number $n_m = \beta^2$ on the detuning $\delta\omega = \omega_0 - \omega$ for the different values of the dimensionless magnetic field $B \equiv \gamma_e B/\omega$ and $\delta_K = \left(\frac{2D^2\omega_f}{\omega_f^2 + \gamma_f^2} - 2K\right)$. In particular, solid lines correspond to $\delta_k = 0$, while dashed lines to $\delta_k = 0.03$ and the dot lines to $\delta_k = -0.03$. The red color corresponds to the dimensionless magnetic field $B \equiv \gamma_e B/\hbar\omega$, $B^2 = 0.1$, the green color to $B^2 = 0.2$, and the blue color to $B^2 = 0.3$.

It is easy to see that in the limit of small $\delta_k \ll 1$ in the fixed point

$$\beta_{01}^2 = \frac{B^2}{\delta\omega^2 + \gamma_m^2}. \quad (17)$$

Then the set of parameters $[\alpha_{01}^4 = D\beta_{01}^4/(\omega_f^2 + \gamma_f^2)$, $\phi = -\pi/2$, $\varphi_{01} = \arctan((\delta\omega - 2D\alpha_{01} - 2K\beta_{01}^2)/\gamma_m)]$, we easily find from Eq.(13). In the nonlinear case our interest concerns two driving frequencies of the external magnetic field

$$\omega_0^{(1,2)} = \omega - 2\delta_k\beta^2 \mp \sqrt{(\delta_k\beta^2)^2 - \gamma_m^2}. \quad (18)$$

In the nonlinear case, the set of the amplitude-frequency characteristic equations

$$\begin{aligned} \delta\omega_{1,2} &= -2\delta_k\beta^2 \mp \sqrt{(\delta_k\beta^2)^2 - \gamma_m^2}, \\ \beta^2 [\gamma_m^2 + (\beta^2\delta_k + \delta\omega)] &= B^2, \end{aligned} \quad (19)$$

has two different solutions $\beta_{1,2}^\pm(\delta\omega)$ for each $\delta\omega = \omega_0^{(1,2)} - \omega$ as it is shown in the $\beta(\delta\omega)$ plot below. The dependence of the steady-state mean magnon number on the detuning $n_m = \beta^2(\delta\omega)$ is plotted in Fig.3. For $\delta_K = \left(\frac{2D^2\omega_f}{\omega_f^2 + \gamma_f^2} - 2K\right) = 0$, we have a linear regime in the system. All three solid lines show that the steady-state mean magnon number depends on the magnetic

field B and increases with B . Condition $\delta_k = 0$ defines the specific values of the external electric field $E = D/g_{ME}$ when the dynamic in the system is linear. For nonzero values of δ_k , dynamic in the system is non-linear, and for every single value of detuning $\delta\omega$, we have two specific values of the steady-state mean magnon numbers $[\beta_{1,2}^\pm(\delta\omega)]^2 = n_m^\pm(1,2) = \langle \hat{m}^+ \hat{m} \rangle_{1,2}^{(\pm)}$. Indexes 1,2 here correspond to the negative and positive detuning cases. The jumps between magnon numbers $\Delta\beta^2 = [\beta_{1,2}^+(\delta\omega)]^2 - [\beta_{1,2}^-(\delta\omega)]^2 = \Delta n_m(1,2)$ depend on the values of detuning. Besides, we clearly see the mirror symmetry $\delta_k \rightarrow -\delta_k$ between dashed and dotted lines. In what follows, we explore the magnon-photon entanglement in the vicinity of both bifurcation points $\beta_{1,2}^\pm(\delta\omega)$. We note that the fixed point value is related to the mean magnon number in the system $[\beta_{1,2}^\pm(\delta\omega)]^2 = n_m^\pm(1,2) = \langle \hat{m}^+ \hat{m} \rangle_{1,2}^{(\pm)}$. Therefore, bifurcation jumps $\Delta\beta^2 = [\beta_{1,2}^+(\delta\omega)]^2 - [\beta_{1,2}^-(\delta\omega)]^2 = \Delta n_m(1,2)$ define the mean magnon number jumps in the system near the bifurcation points. Bifurcations in the system and jumps in the steady-state mean magnon numbers exert a certain impact on the magnon-photon entanglement. Our next aim is to explore steady state mean magnon number as a function of the magnetic field. Taking into account Eq.(13) we deduce the closed polynomial equation for the equilibrium magnon number

$$\begin{aligned} P(\beta) &= \delta_k^2\beta^6 + 2\delta\omega\delta_k\beta^4 + \\ &(\gamma_m^2 + \delta\omega^2)\beta^2 - B^2 = 0. \end{aligned} \quad (20)$$

Analyses of the roots of $P(\beta)$ and derivatives $\partial_x P(x) = 0$, $\partial_{xx} P(x) = 0$, $x \equiv \beta^2$ show the magnon number instability interval as a function of the magnetic field B . Namely, the equation

$$\frac{dP(\beta^2)}{d\beta^2} = 3\delta_k^2\beta^4 + 4\delta\omega\delta_k\beta^2 + (\gamma_m^2 + \delta\omega^2) = 0, \quad (21)$$

for $\delta\omega^2 \geq 3\gamma_m^2$ has two roots

$$\beta_{1,2}^2 = -\frac{2\delta\omega}{3\delta_k} \pm \frac{1}{3\delta_k} \sqrt{\delta\omega^2 - 3\gamma_m^2}. \quad (22)$$

The equations

$$\begin{aligned} P(\beta_{1,2}^2) &= -\frac{2}{27\delta_k} \delta\omega(\delta\omega^2 + 9\gamma_m^2) \pm \\ &\frac{2}{27\delta_k} (\delta\omega^2 - 3\gamma_m^2)^{3/2} - B^2 = 0, \end{aligned} \quad (23)$$

define constraints between parameters in the vicinity of the fixed point:

$$B_{1,2}^2 = \frac{2(-\delta\omega(\delta\omega^2 + 9\gamma_m^2) \pm (\delta\omega^2 - 3\gamma_m^2)^{3/2})}{27\delta_k}. \quad (24)$$

After solving Eq.(24) with respect to the detuning $\delta\omega$ we obtain an equation for the boundary of the instability

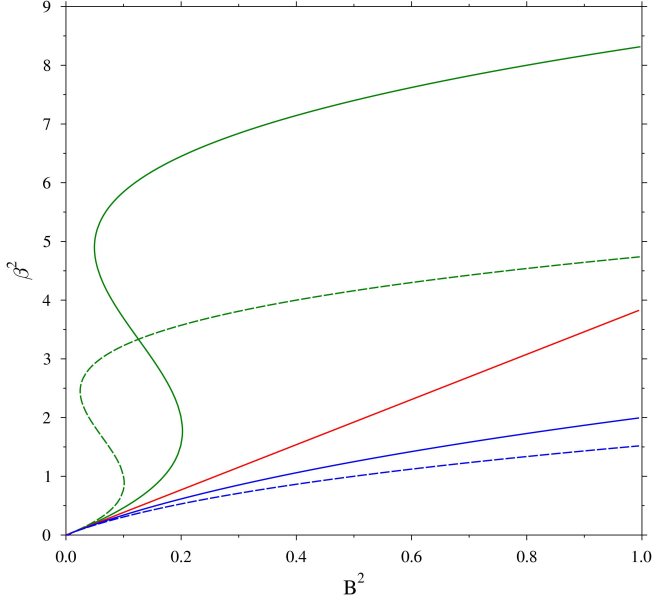


FIG. 4. Dependence of the steady-state mean magnon number $n_m = \beta^2$ on the external dimensionless magnetic field $B \equiv \gamma_e B/\omega$ for the fixed detuning $\delta\omega = \omega_0 - \omega = 0.5$ and the different values of $\delta_k = \left(\frac{2D^2\omega_f}{\omega_f^2 + \gamma_f^2} - 2K\right)$. In particular, the red solid lines corresponds to $\delta_k = 0$, while the green solid and green dashed lines to $\delta_k = -0.1$ and $\delta_k = -0.2$ respectively. The blue solid line corresponds to $\delta_k = 0.1$ and the blue dashed line to $\delta_k = 0.2$. Because of the $n_m(B^2, -\delta_k, \delta\omega) = n_m(B^2, \delta_k, -\delta\omega)$, the plot for the negative detuning $\delta\omega = -0.5$ is the same upon the exchange of green and blue colors.

region in the parametric space $(\delta\omega, D/\sqrt{\omega_f^2 + \gamma_f^2})$ as it follows:

$$\begin{aligned} \Sigma(\delta\omega) = & \delta\omega^4 + \frac{B^2\delta_k}{\gamma_m^2}\delta\omega^3 + 2\gamma_m^2\delta\omega^2 + 9B^2\delta_k\delta\omega + \\ & \frac{27}{4\gamma_m^2}(B^2\delta_k)^2 + \gamma_m^4. \end{aligned} \quad (25)$$

Eq.(25) has two real roots for $\frac{2D^2\omega_f}{\omega_f^2 + \gamma_f^2} - 2K \leq \frac{8\sqrt{3}\gamma_m^3}{9B^2}$ and complex roots otherwise. The jump in the mean magnon number calculated along the borderline of the instability region reads:

$$\Delta n_m = \Delta\beta^2 = \frac{\sqrt{\delta\omega^2 - 3\gamma_m^2}}{2(D^2\omega_f/(\omega_f^2 + \gamma_f^2) - K)}. \quad (26)$$

The steady-state mean magnon number as a function of the external magnetic field $n_m(B) = \beta^2(B)$ is plotted in Fig.4. The red line corresponds to the border of linear regime $\delta_k = 0$ meaning the particular value of the external electric field $E = \sqrt{k(\omega_f^2 + \gamma_f^2)/(\omega_f g_{ME})}$. The green lines correspond to the nonlinear regime. We clearly see the region where two or more values of magnon number

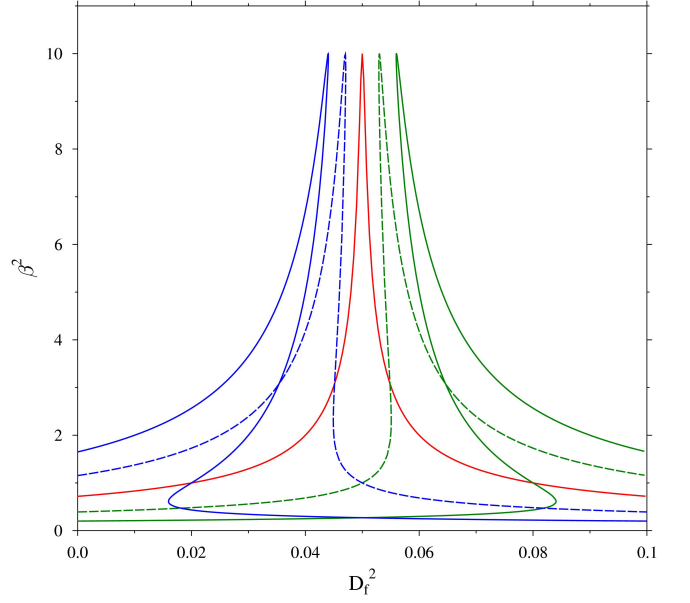


FIG. 5. Dependence of the steady-state mean magnon number $n_m = \beta^2$ on the external electric field $E = D_f/g_{ME}$, $D_f = D/\sqrt{\omega_f^2 + \gamma_f^2}$ for the constant magnetic field $B^2 = 0.1$ and the different values of the detuning: $\delta\omega = 0$ (red solid), $\delta\omega = -0.6$ (green solid), $\delta\omega = -0.3$ (green dashed), $\delta\omega = 0.6$ (blue solid).

β^2 correspond to the single value of the magnetic field. We note that the equation Eq.(20) possesses certain symmetry with respect to the simultaneous transformations $\delta\omega \rightarrow -\delta\omega$ and $\delta_k \rightarrow -\delta_k$. Therefore, linear and nonlinear regimes plotted in Fig.4 by blue and green lines for the positive $\delta\omega = 0.5$, mutually exchange for the negative detuning $\delta\omega = -0.5$ case. In Fig.5 we plot mean magnon number as a function of the applied external electric field. As we see from Fig.5 by proper tuning of the electric field mean magnon number can be increased drastically.

In essence, results shown in Fig.3, Fig.4 and Fig.5 define the borderlines between stability and instability regions. Maps of those regions in the parametric space of applied external fields (D_f, B) , $E = D_f/g_{ME}$, $D_f = D/\sqrt{\omega_f^2 + \gamma_f^2}$ are plotted in Fig.6. Same regions in the parametric space $(\delta\omega, D_f)$ of the detuning $\delta\omega = \omega - \omega_0$ and the electric field are plotted in Fig.7. The change of the sign of the detuning leads to the mirror reflection with respect to the line $\delta_k = 0$.

For visual control and better clarity finally we plot instability regions in 3D plots Fig.8 and Fig.9. The inset lines correspond to the instability and stability regions respectively.

The fixed point of the nonlinear system defines the system's steady state. However, one can pump an arbitrary number of magnons into the system through the nanoantenna and prepare a non-equilibrium state. Non-equilibrium effects are also in the scope of our interest,

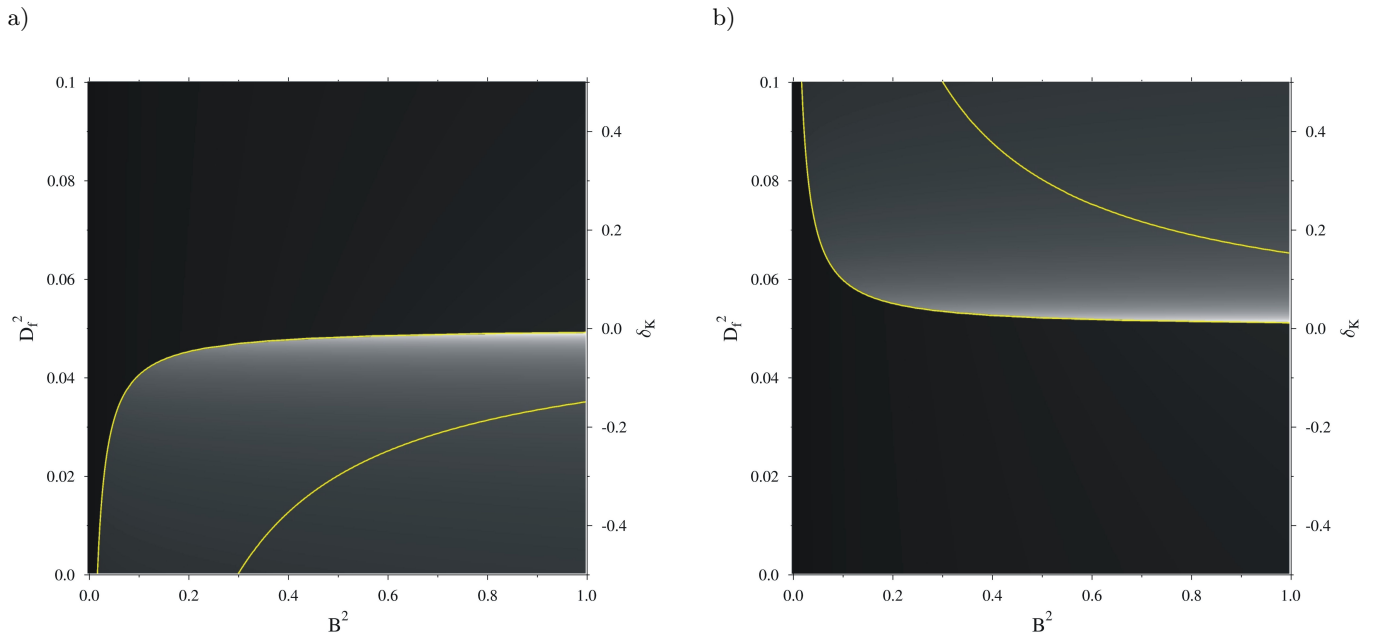


FIG. 6. The map of the steady-state mean magnon number $n_m = \beta^2$ in the parameter space of the external electric $E = D_f/g_{ME}$, $D_f = D/\sqrt{\omega_f^2 + \gamma^2}$ and magnetic fields B . The greyscale defines the value of the mean magnon number. Black corresponds to $n_m = 0$ and white corresponds to $n_m = \max$. Yellow lines define the boundaries of the bistability region for the detuning $\delta\kappa$. The values of detuning are: a) $\delta\omega = 1.0$, b) $\delta\omega = -1.0$.

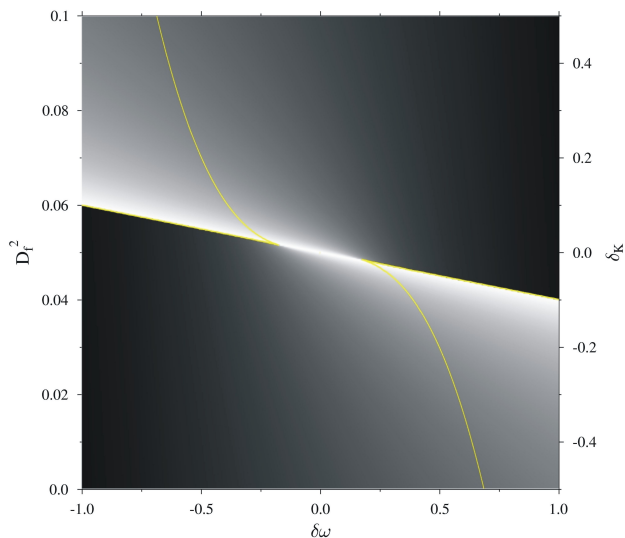


FIG. 7. The map of the steady-state mean magnon number $n_m = \beta^2$ in the parameter space of the external electric field $E = D_f/g_{ME}$, $D_f = D/\sqrt{\omega_f^2 + \gamma^2}$ and the detuning $\delta\omega = \omega_0 - \omega$ between magnon frequency ω and the frequency of the time-dependent magnetic field ω_0 . The greyscale defines the value of the mean magnon number. Black corresponds to $n_m = 0$ and white corresponds to $n_m = \max$. Yellow lines define the boundaries of the bistability region for the value of magnetic field $B^2 = 0.2$.

and therefore, when analyzing nonlinear effects, we exploit more general formalism and study the system's dynamics not only in the vicinity of the steady state fixed point but also in the vicinity of non-equilibrium states.

We proceed with the analysis of the phase space of the dynamical system Eq.(12). We linearize Eq.(12) in the vicinity of the equilibrium point and write down the system of linearized equations:

$$\begin{aligned} \dot{\mathbf{x}} &= \mathbf{F}, \\ \mathbf{x} &= \{\alpha, \phi, \beta, \varphi\}, \quad \mathbf{F} = \{f_1(\mathbf{x}) \dots f_4(\mathbf{x})\}. \end{aligned} \quad (27)$$

While the dimension of set Eq.(27) is $n = 4$, it is characterized by $n + 2$ topologically different types of trajectories. One of them corresponds to the trajectory with a regular fixed point, and the rest $n + 1$ trajectories are characterized by exceptional fixed points (e.g. Saddles, Nodes, Stable spiral, and Unstable spiral) which following Petrovsky [53] we denote by $\mathcal{O}^{p,q}$, where $p = 0, 1, \dots, n$ and $p + q = n$. The points $\mathcal{O}^{p,q}$ with $p \neq n$ are saddle fixed points. The fixed points are found from the condition $\dot{\mathbf{x}} = 0$, i.e., $\mathbf{F}(\mathbf{x}^*) = 0$. The corresponding characteristic equation in the vicinity of \mathbf{x}^* point reads:

$$\chi(\lambda) = \text{Det} \left\| \mathbf{A} - \mathbf{I}\lambda \right\| = \text{Det} \left\| \frac{\partial f_i}{\partial x_j} - \delta_{ij}\lambda \right\| = 0. \quad (28)$$

Here \mathbf{I} is the $(4 \otimes 4)$ identity matrix. The equilibrium state $\mathbf{x}^*[B, D, K]$ is the root of the equation

$$\mathbf{F}(\mathbf{x}^*[B, D, K]) = 0. \quad (29)$$

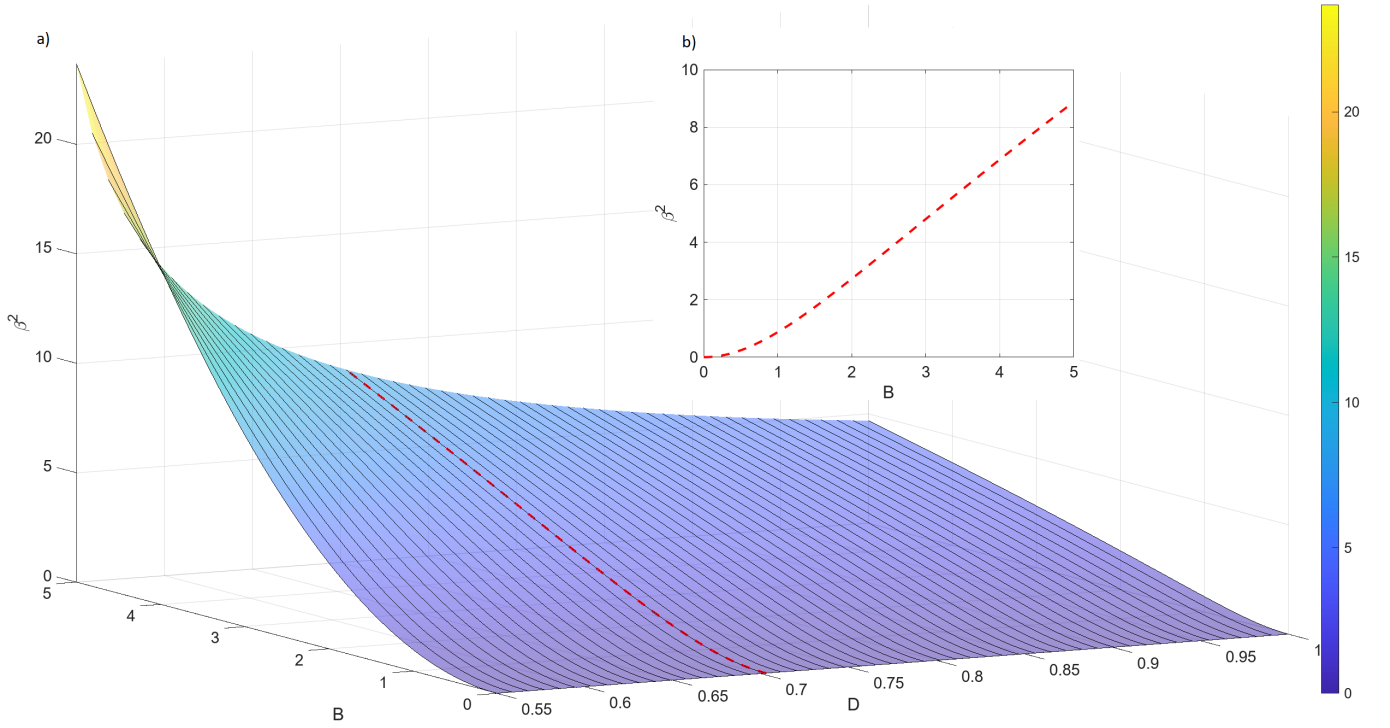


FIG. 8. a) The mean magnon number β^2 in the steady-state, as a function of applied external magnetic and electric fields B , D . b) The inset line shows the dependence of β^2 on B for the fixed value of $D = 0.7$. As we can see, dependence is monotonic, corresponding to the linear regime. The values of the parameters read: $K = 0.06$, $\delta\omega = 1.0$, $\omega_f = 5.0$, $\gamma_f = \gamma_m = 0.1$.

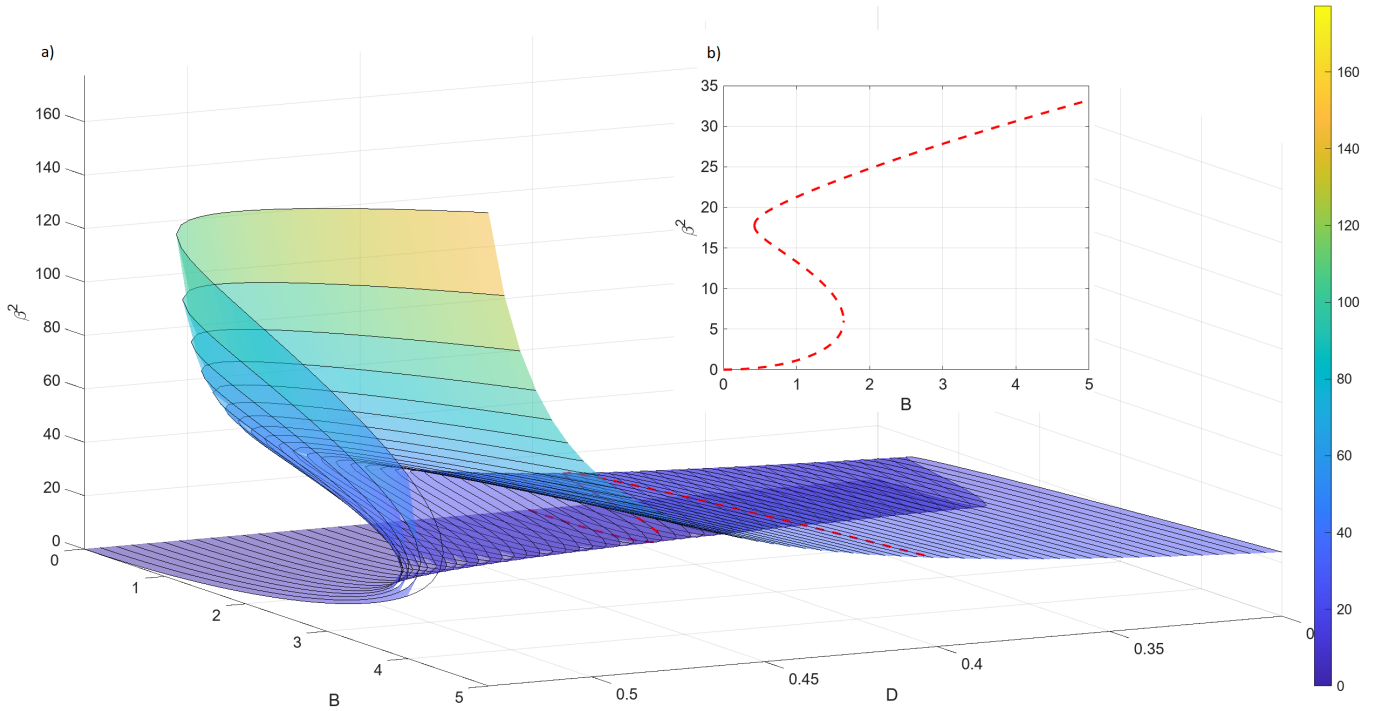


FIG. 9. a) The mean magnon number β^2 in the steady-state, as a function of applied external magnetic and electric fields B , D . The inset line shows the dependence of β^2 on B for the fixed value of $D = 0.4$. We can see that dependence is not monotonic, corresponding to the linear regime. b) The bistability region appears in the interval $0.3 < B < 1.6$. The values of the parameters read: $K = 0.06$, $\delta\omega = 1.0$, $\omega_f = 5.0$, $\gamma_f = \gamma_m = 0.1$.

The type of the exceptional point is defined from the equation

$$\chi(\mathbf{x}^*[B, D, K]) = 0. \quad (30)$$

The border of the equilibrium domain is given by

$$\text{Im}(\lambda = i\Omega) = 0. \quad (31)$$

In essence Eq.(31) defines a hypersurface \mathcal{N}_Ω . We also define the hypersurface $\mathcal{N}_{\Omega=0} = \mathcal{N}_0$ and analyze what happens with the system when phase trajectory crosses

hypersurface. Crossing of \mathcal{N}_0 when steering the parameters of the system demolishes the saddle fixed point $\mathcal{O}^{p,q}$ due to the merging with the states $\mathcal{O}^{p+1,q-1}$ or $\mathcal{O}^{p-1,q+1}$. On the other hand, $\mathcal{O}^{p,q}$ is stable when crossing \mathcal{N}_Ω . We implement this theoretical scheme to our system. After linearization of Eq.(12) $\mathbf{X} = (\delta\alpha, \delta\phi, \delta\beta, \delta\varphi)^T$, where $\delta\alpha = \alpha - \alpha_1$, $\delta\phi = \phi - \phi_1$, $\delta\beta = \beta - \beta_1$, $\delta\varphi = \varphi - \varphi_1$, in the vicinity of arbitrary fixed point $(\alpha_1, \phi_1, \beta_1, \varphi_1)$ we obtain matrix equation:

$$\frac{d\mathbf{X}}{dt} = \mathcal{A}_1 \cdot \mathbf{X}, \quad (32)$$

where matrix \mathcal{A}_1 in the explicit form reads:

$$\begin{pmatrix} \delta\dot{\alpha} \\ \delta\dot{\phi} \\ \delta\dot{\beta} \\ \delta\dot{\varphi} \end{pmatrix} \begin{pmatrix} -\gamma_f & D\beta_1^2 \sin \phi_1 & -2D\beta_1 \cos \phi_1 & 0 \\ -\frac{D\beta_1^2}{\alpha_1^2} \sin \phi_1 & \frac{D\beta_1^2}{\alpha_1} \cos \phi_1 & 2\frac{D\beta_1}{\alpha_1} \sin \phi_1 & 0 \\ 0 & 0 & -\gamma_m & -B \sin \varphi_1 \\ 2D \sin \phi_1 & 2D\alpha_1 \cos \phi_1 & \frac{B}{\beta_1^2} \sin \varphi_1 - 4K\beta_1 & -\frac{B}{\beta_1} \cos \varphi_1 \end{pmatrix} \begin{pmatrix} \delta\alpha \\ \delta\phi \\ \delta\beta \\ \delta\varphi \end{pmatrix}. \quad (33)$$

The characteristic roots of the Eq.(33) can be obtained analytically for equal damping case $\gamma_m = \gamma_f = \gamma_0$ which is a physically reasonable assumption:

$$\lambda_{\pm, \pm} = (p \pm \sqrt{\Delta_{\pm}})/2, \quad (34)$$

where $\Delta_{\pm} = p^2 - 4q_{\pm}$, $p = -2\gamma_0$ and $q_{\pm} = \gamma_0^2 - (\chi_1 \pm \sqrt{\chi_1^2 + \chi_2})/2$, $\chi_1 = -\omega_f^2 - [\delta\omega + (\delta_K - 4K)n_m](\delta\omega + \delta_K n_m)$, $\chi_2 = -4\omega_f [4D^2 n_m + \omega_f(\delta\omega + (\delta_K - 4K)n_m)](\delta\omega + \delta_K n_m)$, with $\delta_k = \left(\frac{2D^2\omega_f}{\omega_f^2 + \gamma_f^2} - 2K\right)$ and equilibrium mean magnon number $n_m = \beta_1^2$. Taking into account explicit expressions of the roots we identify the following three cases relevant to our problem:

I. Saddle point. $p < 0$, $\Delta_{\pm} > 0$, $q_{\pm} < 0$, and $\chi_1 \pm \sqrt{\chi_1^2 + \chi_2} > \gamma_0^2$.

II. Stable node. $p < 0$, $\Delta_{\pm} > 0$, $q_{\pm} > 0$, and $\gamma_0^2 > \chi_1 \pm \sqrt{\chi_1^2 + \chi_2} > 0$.

III. Stable spiral. $p < 0$, $\Delta_{\pm} < 0$, $q_{\pm} > 0$, and $\chi_1 \pm \sqrt{\chi_1^2 + \chi_2} < 0$.

Taking into account definitions below Eq. 34 the cases above can be presented in their reduced form as shown in Table I.

TABLE I. The phase space of the system. As we see, depending on the values of the parameters the system is characterized by Saddle point, Stable node or Stable spiral fixed points.

	Conditions		Phase type
$p < 0$	$\Delta_{\pm} > 4\gamma_0^2$	$q_{\pm} < 0$	Saddle point
$p < 0$	$2\gamma_0^2 < \Delta_{\pm} < 4\gamma_0^2$	$0 < q_{\pm} < \gamma_0^2/2$	Stable node
$p < 0$	$0 < \Delta_{\pm} < 2\gamma_0^2$	$\gamma_0^2/2 < q_{\pm} < \gamma_0^2$	Stable node
$p < 0$	$\Delta_{\pm} < 0$	$q_{\pm} > \gamma_0^2$	Stable spiral

Thus, depending on the values of the parameters, we can have different types of dynamics specified in Table I. For illustrative purposes, the phase spaces of the system for the different sets of parameters are plotted in Fig.10 and Fig.11. We clearly see that the most significant part of the parameter space belongs to the stable spiral points. The change of the sign of detuning from negative $\delta\omega = \omega_0 - \omega = -0.2$ to positive $\delta\omega = 0.2$ shifts the region of stable node and stable spiral points from the small positive $\delta_k = \left(\frac{2D^2\omega_f}{\omega_f^2 + \gamma_f^2} - 2K\right)$ to the slight negative δ_k . The effect observed in Fig.10 means that the system's dynamic can be controlled through the frequency of the time-dependent magnetic field ω_0 and amplitude of the external electric field $E = D/g_{ME}$. With the increase of the of the detuning $\delta\omega$, Fig.11, the saddle point's region becomes larger. Nevertheless, the symmetry upon simultaneous flips of signs $\delta\omega \rightarrow -\delta\omega$ and $\delta_K \rightarrow -\delta_K$ still holds.

Further interest concerns the case $\chi_1^2 + \chi_2 < 0$. Then

$$\begin{aligned} \lambda_{\pm, \pm} &= \text{Re}(\lambda_{\pm, \pm}) + i\text{Im}(\lambda_{\pm, \pm}), \\ \text{Re}(\lambda_{\pm, \pm}) &= \frac{1}{2} \left(p^2 \pm \sqrt{|\Delta'_{\pm}|^2 + |\Delta''_{\pm}|} \cos \xi \right), \\ \text{Im}(\lambda_{\pm, \pm}) &= \frac{1}{2} \sqrt{|\Delta'_{\pm}|^2 + |\Delta''_{\pm}|} \sin \xi, \end{aligned} \quad (35)$$

where

$$\begin{aligned} \Delta'_{\pm} &= \chi_1/2, \quad \Delta''_{\pm} = \sqrt{|\chi_1^2 + \chi_2|}/2, \\ \xi &= \arctan(\Delta''_{\pm}/\Delta'_{\pm}). \end{aligned} \quad (36)$$

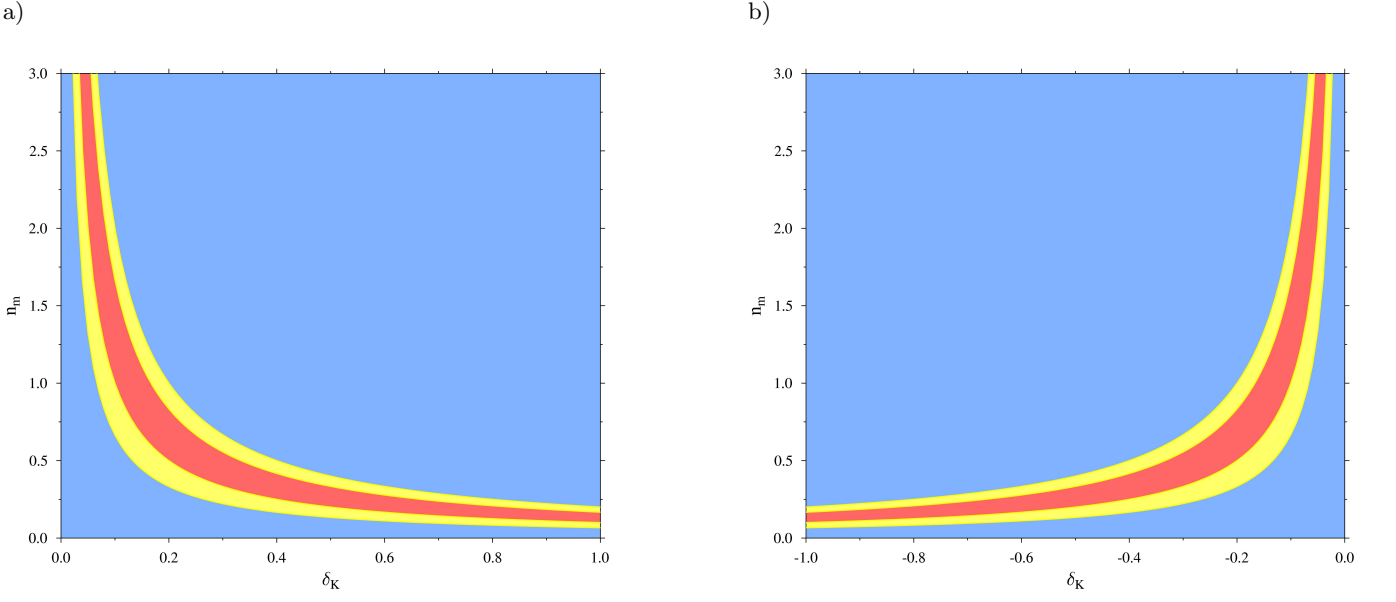


FIG. 10. The map of exceptional fixed points plotted for the value of detuning $\delta\omega$. The region of saddle points is highlighted in red. The map of the region of stable node points is highlighted in yellow. The map of the region of stable spiral points is highlighted in blue. On the x axis $\delta_k = \left(\frac{2D^2\omega_f}{\omega_f^2 + \gamma_f^2} - 2K\right)$ and on the y axis mean magnon number $n_m = \beta^2$. The values of detuning are: a) $\delta\omega = -0.2$, b) $\delta\omega = 0.2$.

IV. Hopf Bifurcation. Hopf bifurcation occurs when $\text{Re}(\lambda_{\pm,\pm})$ changes the sign from negative to positive and characteristic root crosses the imaginary axis. The values of the parameters $D, K, \omega, \omega_0, \omega_f, B, \gamma_0, n_m = \beta_1^2$ for each four cases is shown in the Table II. Considering the case $D = \sqrt{3K(\omega_f^2 + \gamma_f^2)}/\omega_f$ from $\chi_1^2 + \chi_2 < 0$ we deduce:

$$D^2 > \frac{\omega_f^4 + \delta\omega^2(\delta\omega + \delta_K n_m)^2}{16n_m\omega_f(\delta\omega + \delta_K n_m)} - \frac{\omega_f^2\delta\omega}{8n_m}. \quad (37)$$

Or in the resonant case $\delta\omega = 0$:

$$D > \frac{\omega_f\sqrt{\omega_f}}{4n_m\sqrt{\delta_K}}. \quad (38)$$

Together with $D = \sqrt{3K(\omega_f^2 + \gamma_f^2)}/\omega_f$, Eq.(37) and Eq.(38) define bifurcation values of DMI constant. The particular values of the parameters for Hopf bifurcation for the general case are shown in the table II. The analytic solution of the system Eq.(32) reads:

$$\begin{aligned} \delta\alpha(t) &= \sum_{m=\alpha,\phi,\beta,\varphi} C_m \gamma_{m\alpha} \exp[\lambda_m t], \\ \delta\phi(t) &= \sum_{m=\alpha,\phi,\beta,\varphi} C_m \gamma_{m\phi} \exp[\lambda_m t], \\ \delta\beta(t) &= \sum_{m=\alpha,\phi,\beta,\varphi} C_m \gamma_{m\beta} \exp[\lambda_m t], \\ \delta\varphi(t) &= \sum_{m=\alpha,\phi,\beta,\varphi} C_m \gamma_{m\varphi} \exp[\lambda_m t]. \end{aligned} \quad (39)$$

Here $\gamma_{nm} = (-1)^{1+m} \mathcal{M}_{1,m} \{||\mathcal{A} - \mathbf{I}\lambda_n||\}$ is the co-factor of the minor of matrix Eq.(33) and coefficients C_m are defined from the initial conditions.

V. ENTANGLEMENT

To find steady state robust magnon-photon entanglement in the system we follow the recent work [15]. Entanglement is quantified through the logarithmic negativity [22, 25]:

$$E_N = \max[0, -\ln[2\eta^-]], \quad (40)$$

where

$$\eta^- = 2^{-1/2} \{\Sigma(V_1) - [\Sigma(V_1)^2 - 4 \det V_1]^{1/2}\}^{1/2} \quad (41)$$

$$\Sigma(V_1) = \det G_1 + \det B_1 - 2 \det C_1, \quad (42)$$

and the matrix \mathbf{V}_1 is defined as follows:

$$\begin{aligned} \mathcal{A}_1 \mathbf{V}_1 + \mathbf{V}_1 \mathcal{A}_1^T &= \mathbf{W}, \\ \mathbf{V}_1 &= \begin{pmatrix} \mathbf{G}_1 & \mathbf{C}_1 \\ \mathbf{C}_1^T & \mathbf{B}_1 \end{pmatrix}. \end{aligned} \quad (43)$$

The explicit form of the matrix \mathcal{A}_1 is given in Eq.(33), and $\mathbf{W} = -\text{diag}[\gamma_f(2N_f(\omega_f) + 1), \gamma_f(2N_f(\omega_f) + 1), \gamma_m(2N_m(\omega) + 1), \gamma_m(2N_m(\omega) + 1)]$, where $N(\omega) = [\exp(\hbar\omega/k_B T) - 1]^{-1}$ is the boson distribution function.

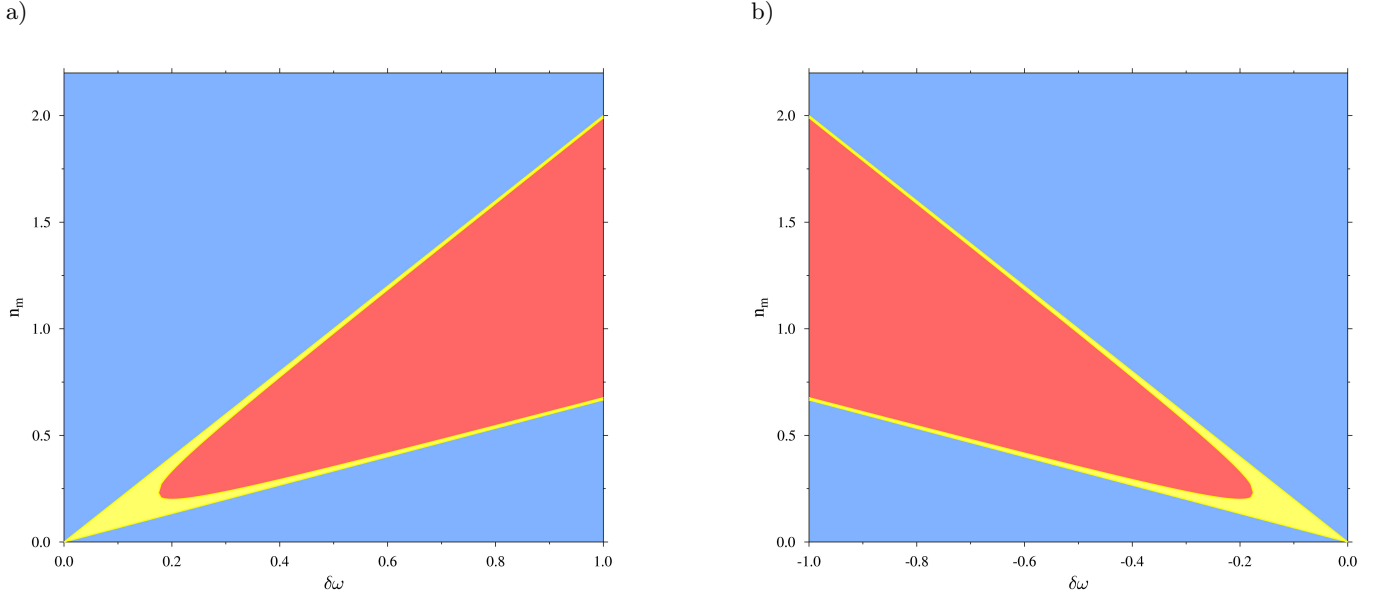


FIG. 11. The map of exceptional fixed points. The region of saddle points is highlighted in red. The map of the region of stable node points is highlighted in yellow. The map of the region of stable spiral points is highlighted in blue. On the x axis is shown detuning $\delta\omega = \omega_0 - \omega$ between the frequency of time dependent magnetic field ω_0 and magnon frequency ω . On the y axis, mean magnon number $n_m = \beta^2$. The values of $\delta_k = \left(\frac{2D^2\omega_f}{\omega_f^2 + \gamma_f^2} - 2K\right)$ are: a) $\delta_k = -0.5$, b) $\delta_k = 0.5$.

TABLE II. Parameters for which specific states of phase space exist.

	β^2	D	K	ω_f	ω_0	ω	$\gamma_0 = \gamma_m = \gamma_f$
I. Saddle point	30	0.16	0.06	0.5	2.5	5.5	0.1
	30	0.20	0.06	0.5	2.5	5.5	0.1
	30	0.23	0.06	0.5	2.5	5.5	0.1
	30	0.18	0.06	0.5	2.0	2.5	0.1
	30	0.20	0.06	0.5	2.0	2.5	0.1
	30	0.25	0.06	0.5	2.0	2.5	0.1
	25	0.18	0.06	0.5	2.0	2.5	0.1
	25	0.20	0.06	0.5	2.0	2.5	0.1
	25	0.25	0.06	0.5	2.0	2.5	0.1
II. Stable node	30	0.32	0.06	1.0	0.2	5.0	10
	30	0.33	0.06	1.0	0.2	5.0	10
	30	0.34	0.06	1.0	0.2	5.0	10
	25	0.30	0.06	1.0	0.2	5.0	10
	25	0.31	0.06	1.0	0.2	5.0	10
III. Stable spiral	25	0.60	0.06	5.0	1.0	1.5	0.1
	25	0.55	0.06	5.0	1.0	1.5	0.1
	25	0.20	0.06	5.0	1.0	1.5	0.1
	30	0.20	0.06	5.0	1.0	1.5	0.1
	30	0.40	0.06	5.0	1.0	1.5	0.1
	30	0.55	0.06	5.0	1.0	1.5	0.1
	30	0.20	0.06	5.0	0.5	1.5	0.1
	30	0.40	0.06	5.0	0.5	1.5	0.1
	30	0.55	0.06	5.0	0.5	1.5	0.1
IV. Hopf bifurcation	20	0.9489	0.06	5.0	1.0	2.0	0.1
	25	0.9489	0.06	5.0	1.0	2.0	0.1
	30	0.9489	0.06	5.0	1.0	2.0	0.1
	30	0.8488	0.06	4.0	1.0	2.0	0.1
	25	0.8488	0.06	4.0	1.0	2.0	0.1
	20	0.8488	0.06	4.0	1.0	2.0	0.1

Results of numerical calculations for the entanglement are plotted in Fig.12. In Fig.12 we see two drop-shaped

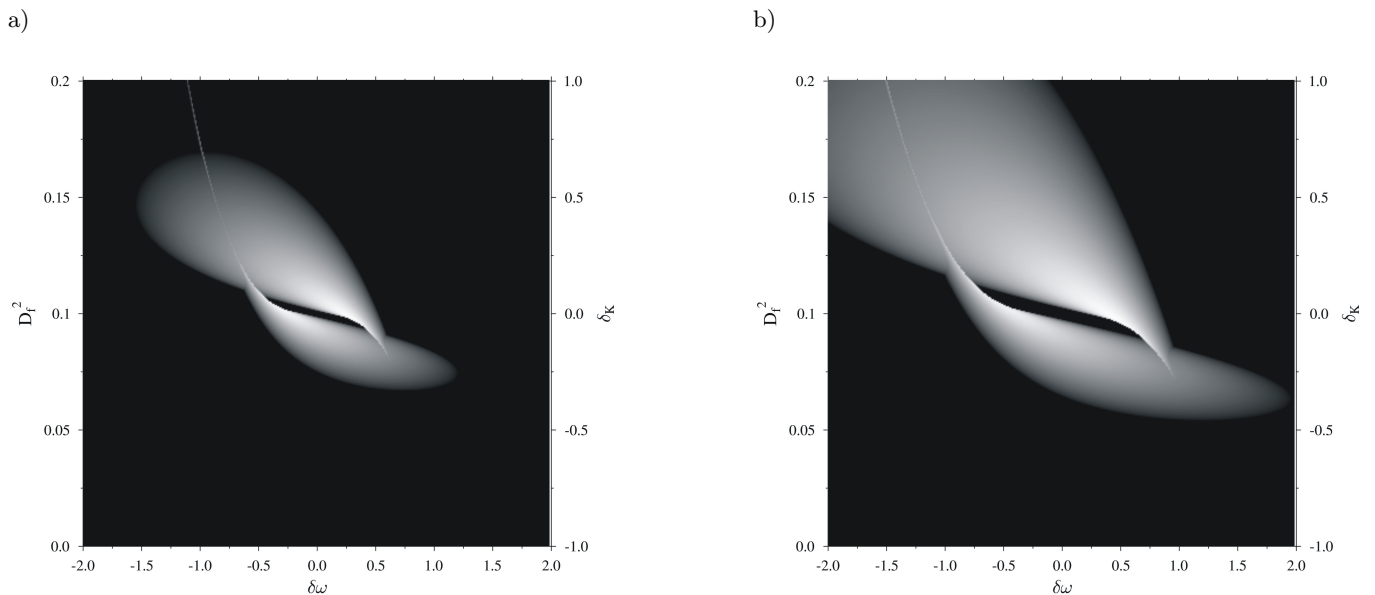


FIG. 12. Dependence of entanglement on the detuning $\delta\omega = \omega_0 - \omega$ and parameter $\delta_k[D_f] = 2D_f^2\omega_f - 2K$, where $D_f = D/\sqrt{\omega_f^2 + \gamma_f^2}$. The white color corresponds to the nonzero entanglement region. The temperature in the system $T = 0.1$ Kelvin, meaning that $k_B T = \hbar\omega/2$. The values of the dimensionless magnetic field $B \equiv \gamma_e B/\omega$ are: a) $B^2 = 0.2$, b) $B^2 = 0.5$.

regions of nonzero entanglement. Surprisingly, we see the symmetry breaking concerning the mutual flip of the signs $(\delta\omega, \delta_k) \rightarrow (-\delta\omega, -\delta_k)$. The sizes of two nonzero entanglement regions are different. The reason for the observed asymmetry is the fact that not only the difference between magnon frequency ω and the frequency of the external magnetic field ω_0 is essential but the value of the magnon frequency ω as well. Hence, the determination of the entanglement cannot be reduced solely to the value of detuning $\delta\omega = \omega_0 - \omega$. As a consequence, the quantum properties of the system are characterized by symmetry lower than in the classical case Eq.(20).

The green lines plotted in Fig. 13 correspond to the $\delta_k = -0.03$ section (Fig. 13a) and the $\delta_k = 0.03$ section (Fig. 13b) of central part of Fig. 12a. The central broad maximum of the entanglement is associated with the small detuning case $|\delta\omega| < 0.2$, while the side sharp maximum in the vicinity of $\delta\omega = \pm 0.4$ is counter intuitive. Upon flipping the sign of the detuning the maximal value of the entanglement associated with the sizeable detuning case is almost the same. Comparing the results for the entanglement plotted in Fig.12 and Fig.13 with the phase portrait of the system Fig.10 and Fig.11, we conclude that the most significant values of the entanglement are linked with the border between Stable spiral and Stable node fixed point regions. In the red region (the Saddle fixed point region), the logarithmic negativity becomes imaginary, meaning that the entanglement is not defined in the Saddle fixed point region.

In Fig.14, we plot the magnon-photon entanglement as a function of the applied external magnetic and electric fields $B, D = g_{ME}E$. The white region corresponds to

the nonzero entanglement. As we see, entanglement in the system is zero for a weak electric field case. Comparing Fig.14 with Fig.6, we see that the sign of the detuning between magnon frequency and the frequency of time-dependent magnetic field $\delta\omega = \omega_0 - \omega$ influences the region of nonzero entanglement. Moreover, the sharp maxima of the entanglement are aligned along one of the boundary lines of the bistability region. Also in Fig.12 one can see the trace of bistability border line presented in Fig.7. The yellow lines in Fig.15 correspond to the border between Stable spiral and Stable node regions in Fig.11 (the blue and yellow regions). As we see in Fig.15, the entanglement disappears after crossing the bottom border of the Stable node region and becomes nonzero only after crossing the upper yellow line. A very interesting fact is that the black region between yellow lines with zero entanglement is characterized by singularities of the covariance matrix Eq.(43), and on the other hand, it corresponds to the Saddle point region of the dynamical system Fig.11.

The temperature dependence of the entanglement we infer from Fig.15. Namely, the zero temperature case $k_B T = 0$ is plotted in Fig.15a and Fig.15b correspond for $\delta_K = -0.5$ and $\delta_K = 0.5$ respectively. Fig.15c and Fig.15d correspond to the nonzero temperature case for $\delta_K = -0.5$ (Fig. 15c) and $\delta_K = 0.5$ (Fig. 15d)

As we can see, the nonzero magnon-photon entanglement region shrinks with the increase of temperature.

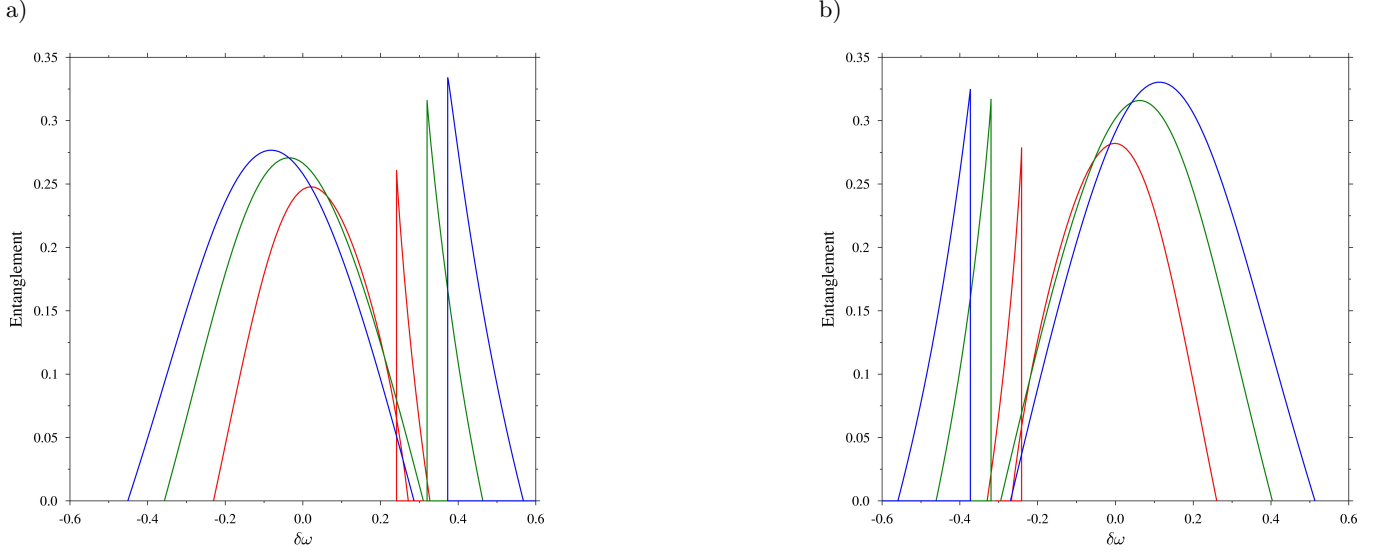


FIG. 13. The dependence of the entanglement on the detuning between the frequency of external time-dependent magnetic field and the magnon frequency $\delta\omega = \omega_0 - \omega$ for the different values of magnetic fields: $B^2 = 0.1$ the red line, $B^2 = 0.2$ the green line, $B^2 = 0.3$ the blue line. The first maximum in the entanglement is associated with the small detuning case $|\delta\omega| < 0.2$, while the second maximum occurs in the vicinity of a) $\delta\omega = 0.4$ and b) $\delta\omega = -0.4$. With the increase of the amplitude of the time dependent magnetic field, the maximum of the entanglement moves towards the higher values of the detuning. This result is straightforward because the weak field in the sizeable detuning limit does not compensate for the thermal decay of magnons. The value of the temperature $T = 0.1$ Kelvin meaning that $k_B T = \hbar\omega/2$. The values of parameter $\delta_k = \left(\frac{2D_f^2\omega_f}{\omega_f^2 + \gamma_f^2} - 2K \right)$ are: a) $\delta_k = -0.03$ b) $\delta_k = 0.03$.

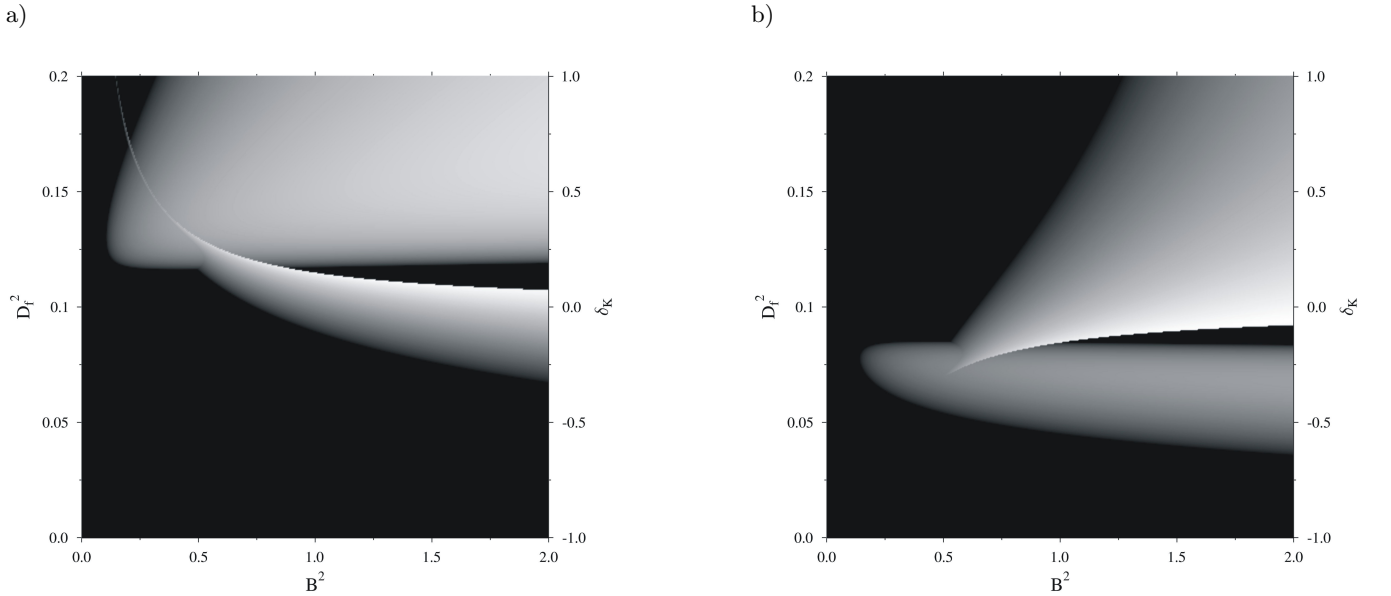


FIG. 14. Dependence of entanglement on the magnetic and electric fields B , D_f and parameter $\delta_k = 2D_f^2\omega_f - 2K$, where $D_f = D/\sqrt{\omega_f^2 + \gamma_f^2}$. The white color corresponds to the nonzero entanglement region. The temperature in the system $T = 0.1$ Kelvin, meaning that $k_B T = \hbar\omega/2$. Detuning between magnon frequency ω and the frequency of the time-dependent magnetic field ω_0 is equal to $\delta\omega = \omega_0 - \omega$. The values of $\delta\omega$ are: a) $\delta\omega = -1\text{GHz}$, b) $\delta\omega = 1\text{GHz}$.

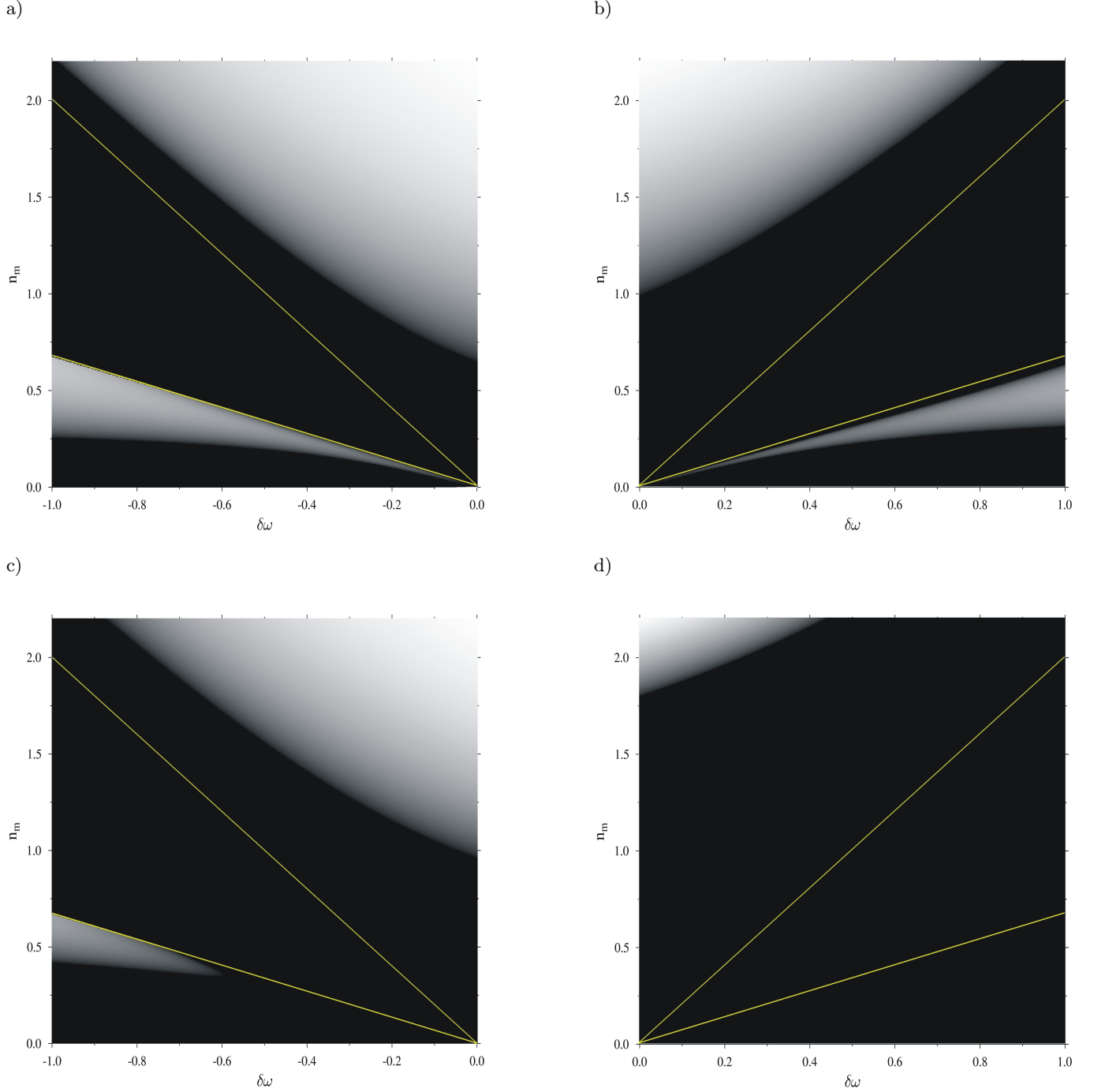


FIG. 15. Dependence of entanglement on the detuning $\delta\omega = \omega_0 - \omega$ and magnon mean number $n_m = \beta^2$. The white color corresponds to the nonzero entanglement region. The yellow lines correspond to the border between Stable spiral and Stable node regions in Fig.11 (the blue and yellow regions). The values of the magnetic field B^2 , parametr $\delta_k = \left(\frac{2D^2\omega_f}{\omega_f^2 + \gamma_f^2} - 2K\right)$ and temperature T in the system are: a) $B^2 = 0.5$, $\delta_k = 0.5$, $T = 0$ Kelvin meaning that $k_B T = 0$, b) $B^2 = 0.5$, $\delta_k = -0.5$, $T = 0$ Kelvin meaning that $k_B T = 0$, c) $B^2 = 0.5$, $\delta_k = 0.5$, $T = 0.1$ Kelvin meaning that $k_B T = \hbar\omega/2$, d) $B^2 = 0.5$, $\delta_k = -0.5$, $T = 0.1$ Kelvin meaning that $k_B T = \hbar\omega/2$.

VI. CONCLUSIONS

In the present project, we studied the optomagnonic crystal system based on the YIG slab with the periodic air holes drilled in the slab. The periodic air holes lead to the optical crystal properties, and for the confinement of the magnonic excitations, we proposed to exploit the magnon condensation effect and intraband magnon-magnon interaction originated from the perpendicular magnetocrystalline anisotropy (PMA) and bismuth doping on the YIG slab. Then, the magnon-magnon interband interaction term in the magnon condensate mimics the effective Kerr effect. The magnonic spectrum has a profound minimum that grants a magnon confinement effect. Overall, confined magnons and photons in the optomagnonic crystal interact through the magneto-electric effect observed for YIG earlier. To quantify the entanglement between two continuous bosonic modes, such as magnons and photons, we followed the state-of-the-art method for today. Using the quantum Langevin equations subjected to thermal noise, we calculated the logarithmic negativity. When using this method in previous studies, the standard recipe was a linearization procedure, i.e., replacing quantum operators by their semiclassical expectation values calculated near the steady state. The cost of this approximation is the loss of information about the phases of propagated quantum states. In the present work, we avoid this linearization procedure and study the impact of the nonlinear effects on the entanglement properties. Namely, in the standard semiclassical approximation, a general quantum operator \hat{Q} is replaced by $\hat{Q} = \langle \hat{Q} \rangle + \delta\hat{Q}$, where $\delta\hat{Q}$ is the deviation of operators from its steady state expectation value $\langle \hat{Q} \rangle$. In particular, magnon creation and annihilation operators are replaced by $\langle \hat{m}^\dagger \rangle = \beta^* e^{-i\varphi}$, $\langle \hat{m} \rangle = \beta e^{i\varphi}$. While the mean magnon number is given by $\langle \hat{m}^\dagger \hat{m} \rangle = |\beta|^2$, the phase φ is considered as a free parameter in the linear theory. The present work showed that phase plays a crucial role in nonlinear cases, leading to the instability and transitions between the different dynamical regimes. Before analyzing the quantum entanglement, we explored the nonlinear semiclassical dynamics in detail and precisely defined the phase space. It is well known that the typical nonlinear dynamical system holds bifurcation points and fixed points of different characters in its phase space: Saddle points, Stable and unstable spiral, and Stable node points. We showed that methods of the qualitative theory of nonlinear differential equations are also relevant for optomagnonic problems. We found that the entanglement is not defined in the Saddle fixed point region (see red region in Fig. 16). On the other hand, we proved that the maximum of the entanglement corresponds to the region near the border between the Stable node and Saddle spiral fixed point regions (the border between yellow and blue regions in Fig. 16)). Besides, we calculated photon modes for a particular geometry of the optomagnonic crystal. We have analyzed the amplitude-frequency characteristics of the optomagnonic crystal and

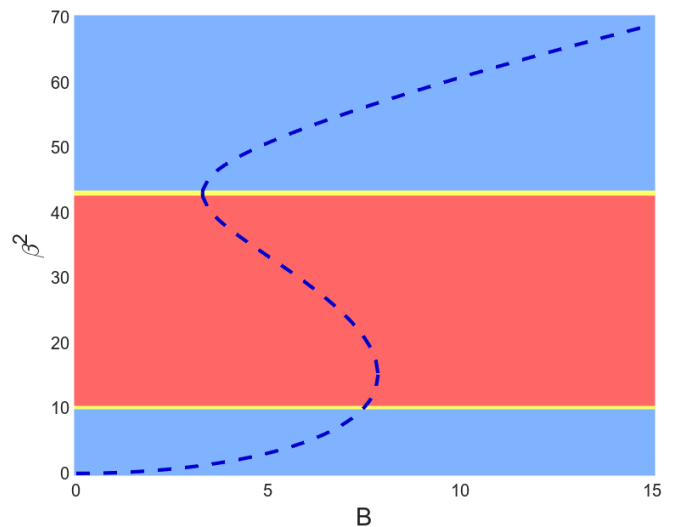


FIG. 16. Schematic dependence of phase spaces on the magnetic field B and the mean magnon number β^2 . The dashed line indicates the dependence of β^2 on B . The region of saddle points is highlighted in red. The map of the region of stable node points is highlighted in yellow. The map of the region of stable spiral points is highlighted in blue. The values of the parameters read: $D = 0.16$, $K = 0.06$, $\omega_f = 0.5$, $\omega_0 = 2.5$, $\omega = 5.5$, $\gamma_f = \gamma_m = 0.5$.

showed that due to the instability region, one could efficiently switch the mean magnon numbers in the system and control entanglement in the system. We discovered that the zero-entanglement region is characterized by the singularity in the covariance matrix and corresponds to the Saddle fixed point region of the dynamical system. We also studied the dependence of magnon-photon entanglement on the temperature and showed that the region of the nonzero entanglement shrinks at higher temperatures. Our primary finding is that the covariance matrix has singularities in the Saddle fixed point region, and therefore, entanglement is not defined in the same region. The entanglement is nonzero in the Stable spiral fixed point region as it is shown schematically in Fig. 16.

-
- [1] H. Huebl, C. W. Zollitsch, J. Lotze, F. Hocke, M. Greifenstein, A. Marx, R. Gross, and S. T. B. Goennenwein, High cooperativity in coupled microwave resonator ferrimagnetic insulator hybrids, *Phys. Rev. Lett.* **111**, 127003 (2013).
- [2] Y. Tabuchi, S. Ishino, T. Ishikawa, R. Yamazaki, K. Usami, and Y. Nakamura, Hybridizing ferromagnetic magnons and microwave photons in the quantum limit, *Phys. Rev. Lett.* **113**, 083603 (2014).
- [3] X. Zhang, C.-L. Zou, L. Jiang, and H. X. Tang, Strongly coupled magnons and cavity microwave photons, *Phys. Rev. Lett.* **113**, 156401 (2014).
- [4] J. A. Haigh, N. J. Lambert, A. C. Doherty, and A. J. Ferguson, Dispersive readout of ferromagnetic resonance for strongly coupled magnons and microwave photons, *Phys. Rev. B* **91**, 104410 (2015).
- [5] J. Graf, S. Sharma, H. Huebl, and S. V. Kusminskiy, Design of an optomagnonic crystal: Towards optimal magnon-photon mode matching at the microscale, *Phys. Rev. Res.* **3**, 013277 (2021).
- [6] A. Bachtold, J. Moser, and M. Dykman, Mesoscopic physics of nanomechanical systems, *Reviews of Modern Physics* **94**, 045005 (2022).
- [7] M. Aspelmeyer, T. J. Kippenberg, and F. Marquardt, Cavity optomechanics, *Reviews of Modern Physics* **86**, 1391 (2014).
- [8] A. Singh, L. Chotorlishvili, Z. Toklikishvili, I. Tralle, and S. Mishra, Hybrid quantum–classical chaotic nems, *Physica D: Nonlinear Phenomena* **439**, 133418 (2022).
- [9] Y. Chougale, J. Talukdar, T. Ramos, and R. Nath, Dynamics of Rydberg excitations and quantum correlations in an atomic array coupled to a photonic crystal waveguide, *Phys. Rev. A* **102**, 022816 (2020).
- [10] M. T. Manzoni, L. Mathey, and D. E. Chang, Designing exotic many-body states of atomic spin and motion in photonic crystals, *Nat. Commun.* **8**, 1 (2017).
- [11] A. Goban, C.-L. Hung, S.-P. Yu, J. Hood, J. Muniz, J. Lee, M. Martin, A. McClung, K. Choi, D. E. Chang, *et al.*, Atom–light interactions in photonic crystals, *Nat. Commun.* **5**, 1 (2014).
- [12] C. Hung, S. Meenehan, D. Chang, O. Painter, and H. Kimble, Trapped atoms in one-dimensional photonic crystals, *New Journal of Physics* **15**, 083026 (2013).
- [13] J. S. Douglas, H. Habibian, C.-L. Hung, A. V. Gorshkov, H. J. Kimble, and D. E. Chang, Quantum many-body models with cold atoms coupled to photonic crystals, *Nature Photonics* **9**, 326 (2015).
- [14] J. Li, S.-Y. Zhu, and G. S. Agarwal, Magnon-phonon entanglement in cavity magnomechanics, *Phys. Rev. Lett.* **121**, 203601 (2018).
- [15] Z. Toklikishvili, L. Chotorlishvili, R. Khomeriki, V. Jandieri, and J. Berakdar, Electrically controlled entanglement of cavity photons with electromagnons, *Phys. Rev. B* **107**, 115126 (2023).
- [16] H. Pan, Y. Yang, Z. H. An, and C.-M. Hu, Bistability in dissipatively coupled cavity magnonics, *Phys. Rev. B* **106**, 054425 (2022).
- [17] M. Wang, C. Kong, Z.-Y. Sun, D. Zhang, Y.-Y. Wu, and L.-L. Zheng, Nonreciprocal high-order sidebands induced by magnon kerr nonlinearity, *Phys. Rev. A* **104**, 033708 (2021).
- [18] Z.-B. Yang, W.-J. Wu, J. Li, Y.-P. Wang, and J. Q. You, Steady-entangled-state generation via the cross-kerr effect in a ferrimagnetic crystal, *Phys. Rev. A* **106**, 012419 (2022).
- [19] C. Kong, H. Xiong, and Y. Wu, Magnon-induced non-reciprocity based on the magnon kerr effect, *Phys. Rev. Appl.* **12**, 034001 (2019).
- [20] G.-Q. Zhang, Y. Wang, and W. Xiong, Detection sensitivity enhancement of magnon kerr nonlinearity in cavity magnonics induced by coherent perfect absorption, *Phys. Rev. B* **107**, 064417 (2023).
- [21] R.-C. Shen, J. Li, Z.-Y. Fan, Y.-P. Wang, and J. Q. You, Mechanical bistability in kerr-modified cavity magnomechanics, *Phys. Rev. Lett.* **129**, 123601 (2022).
- [22] R. Simon, Peres-horodecki separability criterion for continuous variable systems, *Phys. Rev. Lett.* **84**, 2726 (2000).
- [23] L.-M. Duan, G. Giedke, J. I. Cirac, and P. Zoller, Inseparability criterion for continuous variable systems, *Phys. Rev. Lett.* **84**, 2722 (2000).
- [24] M. Hillery and M. S. Zubairy, Entanglement conditions for two-mode states, *Phys. Rev. Lett.* **96**, 050503 (2006).
- [25] G. Adesso and F. Illuminati, Entanglement in continuous-variable systems: recent advances and current perspectives, *Journal of Physics A: Mathematical and Theoretical* **40**, 7821 (2007).
- [26] Q. Y. He, P. D. Drummond, M. K. Olsen, and M. D. Reid, Einstein-Podolsky-Rosen entanglement and steering in two-well bose-einstein-condensate ground states, *Phys. Rev. A* **86**, 023626 (2012).
- [27] T. Liu and G. Vignale, Electric control of spin currents and spin-wave logic, *Phys. Rev. Lett.* **106**, 247203 (2011).
- [28] Y. Yamasaki, Y. Kohara, and Y. Tokura, Quantum magnetoelectric effect in iron garnet, *Phys. Rev. B* **80**, 140412 (2009).
- [29] M. Trybus, L. Chotorlishvili, and E. Jartych, Dielectric and magnetoelectric properties of tgs–magnetite composite, *Molecules* **29**, 1378 (2024).
- [30] S. Kolesnikov and E. Saprónova, Energy barriers for the spontaneous magnetization reversal of atomic co chains on the surface pt (664) in the model of dzyaloshinskii-moriya interaction, *Journal of Surface Investigation: X-ray, Synchrotron and Neutron Techniques* **18**, 150 (2024).
- [31] S. Kolesnikov, E. S. Saprónova, and I. N. Kolesnikova, An influence of the dzyaloshinskii-moriya interaction on the magnetization reversal process of the finite-size co chains on pt (664) surface, *Journal of Magnetism and Magnetic Materials* **579**, 170869 (2023).
- [32] S. V. Kolesnikov and E. S. Saprónova, Influence of dzyaloshinskii-moriya and dipole–dipole interactions on spontaneous magnetization reversal time of finite-length co chains on pt (664) surfaces, *IEEE Magnetics Letters* **13**, 1 (2022).
- [33] X.-G. Wang, L. Chotorlishvili, V. K. Dugaev, A. Ernst, I. V. Maznichenko, N. Arnold, C. Jia, J. Berakdar, I. Mertig, and J. Barnaś, The optical tweezer of skyrmions, *npj Computational Materials* **6**, 140 (2020).
- [34] S. O. Demokritov, V. E. Demidov, O. Dzyapko, G. A. Melkov, A. A. Serga, B. Hillebrands, and A. N. Slavin, Bose–einstein condensation of quasi-equilibrium magnons at room temperature under pumping, *Nature*

- 443, 430 (2006).
- [35] M. Schneider, T. Brächer, D. Breitbach, V. Lauer, P. Pirro, D. A. Bozhko, H. Y. Musiienko-Shmarova, B. Heinz, Q. Wang, T. Meyer, *et al.*, Bose–einstein condensation of quasiparticles by rapid cooling, *Nature Nanotechnology* **15**, 457 (2020).
- [36] M. Mohseni, A. Qaiumzadeh, A. A. Serga, A. Brataas, B. Hillebrands, and P. Pirro, Bose–einstein condensation of nonequilibrium magnons in confined systems, *New Journal of Physics* **22**, 083080 (2020).
- [37] T. Frostad, P. Pirro, A. A. Serga, B. Hillebrands, A. Brataas, and A. Qaiumzadeh, Anisotropy-assisted magnon condensation in ferromagnetic thin films, *Phys. Rev. Res.* **6**, L012011 (2024).
- [38] A. A. Bukharaev, A. K. Zvezdin, A. P. Pyatakov, and Y. K. Fetisov, Straintronics: a new trend in micro-and nanoelectronics and materials science, *Physics-Uspekh* **61**, 1175 (2018).
- [39] S. Stagraczyński, L. Chotorlishvili, M. Schüler, M. Mierzejewski, and J. Berakdar, Many-body localization phase in a spin-driven chiral multiferroic chain, *Phys. Rev. B* **96**, 054440 (2017).
- [40] R. Khomeriki, L. Chotorlishvili, I. Tralle, and J. Berakdar, Positive–negative birefringence in multiferroic layered metasurfaces, *Nano Letters* **16**, 7290 (2016).
- [41] R. Khomeriki, L. Chotorlishvili, B. A. Malomed, and J. Berakdar, Creation and amplification of electromagnon solitons by electric field in nanostructured multiferroics, *Phys. Rev. B* **91**, 041408 (2015).
- [42] X.-G. Wang, L. Chotorlishvili, N. Arnold, V. K. Dugaev, I. Maznichenko, J. Barnaś, P. A. Buczek, S. S. P. Parkin, and A. Ernst, Plasmonic skyrmion lattice based on the magnetoelectric effect, *Phys. Rev. Lett.* **125**, 227201 (2020).
- [43] T. Holstein and H. Primakoff, Field dependence of the intrinsic domain magnetization of a ferromagnet, *Phys. Rev.* **58**, 1098 (1940).
- [44] H. Maier-Flaig, S. Klingler, C. Dubs, O. Surzhenko, R. Gross, M. Weiler, H. Huebl, and S. T. B. Goennewein, Temperature-dependent magnetic damping of yttrium iron garnet spheres, *Phys. Rev. B* **95**, 214423 (2017).
- [45] E. A. Stepanov, C. Dutreix, and M. I. Katsnelson, Dynamical and reversible control of topological spin textures, *Phys. Rev. Lett.* **118**, 157201 (2017).
- [46] A. P. Itin and M. I. Katsnelson, Effective hamiltonians for rapidly driven many-body lattice systems: Induced exchange interactions and density-dependent hoppings, *Phys. Rev. Lett.* **115**, 075301 (2015).
- [47] V. Jandieri, P. Baccarelli, G. Valerio, and G. Schettini, 1-d periodic lattice sums for complex and leaky waves in 2-d structures using higher order ewald formulation, *IEEE Transactions on Antennas and Propagation* **67**, 2364 (2019).
- [48] V. Jandieri, P. Baccarelli, G. Valerio, K. Yasumoto, and G. Schettini, Modal propagation in periodic chains of circular rods: Real and complex solutions, *IEEE Photonics Technology Letters* **32**, 1053 (2020).
- [49] K. Yasumoto and K. Yoshitomi, Efficient calculation of lattice sums for free-space periodic green’s function, *IEEE Transactions on Antennas and Propagation* **47**, 1050 (1999).
- [50] L. Chotorlishvili and A. Ugulava, Quantum chaos and its kinetic stage of evolution, *Physica D: Nonlinear Phenomena* **239**, 103 (2010).
- [51] A. Ugulava, L. Chotorlishvili, and K. Nickoladze, Quantum-mechanical research on nonlinear resonance and the problem of quantum chaos, *Phys. Rev. E* **70**, 026219 (2004).
- [52] A. Ugulava, L. Chotorlishvili, and K. Nickoladze, Irreversible evolution of quantum chaos, *Phys. Rev. E* **71**, 056211 (2005).
- [53] A. Katok, A. Katok, and B. Hasselblatt, *Introduction to the modern theory of dynamical systems*, 54 (Cambridge university press, 1995).
- [54] M. I. Rabinovich and D. I. Trubetskov, *Oscillations and waves: in linear and nonlinear systems*, Vol. 50 (Springer Science & Business Media, 2012).